8-2014

A Study of the Structure of Light Tin Isotopes via Single-Neutron Knockout Reactions

Andrew Franklin Ayres
University of Tennessee - Knoxville, aayres@utk.edu

To the Graduate Council:

I am submitting herewith a dissertation written by Andrew Franklin Ayres entitled "A Study of the Structure of Light Tin Isotopes via Single-Neutron Knockout Reactions." I have examined the final electronic copy of this dissertation for form and content and recommend that it be accepted in partial fulfillment of the requirements for the degree of Doctor of Philosophy, with a major in Physics.

Kate L. Jones, Major Professor

We have read this dissertation and recommend its acceptance:

Robert K. Grzywacz, Witold Nazarewicz, Laurence H. Heilbronn

Accepted for the Council:
Carolyn R. Hodges

Vice Provost and Dean of the Graduate School

(Original signatures are on file with official student records.)

A Study of the Structure of Light Tin Isotopes via Single-Neutron Knockout Reactions

A Dissertation Presented for the

Doctor of Philosophy

Degree

The University of Tennessee, Knoxville

Andrew Franklin Ayres

August 2014

Dedicated to my wife Janna, who has supported me in all that I've done for the past 15 years.

Abstract

The region around ^{100}Sn [100Sn] is important because of the close proximity to the N=Z=50 magic numbers, the rp process, and the proton drip-line. Alpha decay measurements show a reversal in the spin-parity assignments of the ground and first excited states in ^{101}Sn [101Sn] compared to ^{105}Te [105Te]. However, the lightest odd-mass tin isotope with a firm spin-parity assignment is ^{109}Sn [109Sn]. The $d_{5/2}$ [d5/2] and $g_{7/2}$ [g7/2] single-particle states above N=50 are near degenerate, evidenced by the excitation energy of the first excited state in ^{101}Sn at only 172 keV. The correct ordering of these single-particle states and the degree of neutron configuration mixing has been the subject of debate.

Spectroscopic studies have been performed close to ^{100}Sn [100Sn], utilizing the S800 and CAESAR at the NSCL. These studies make use of a single neutron knockout reaction on beams of ^{108}Sn [108Sn] and ^{106}Sn [106Sn]. The momentum distributions of the resulting residues reflect the ℓ-value [l-value] of the removed neutron. Additionally, γ-rays [gamma-rays] were measured in coincidence with the momentum distributions allowing for the separation of the knockout channel where the residue is left in an excited state from the channel to the ground state. The odd-mass residue can then be characterized in terms of a hole in the d- or g- orbital with reference to the even-mass nucleus. The relative population of final states in the odd-mass residue are indicative of the mixing in the ground state of ^{108,106}Sn [108,106Sn].

Comparing the momentum distributions with reaction calculations shows that both ^{105}Sn [105Sn]and ^{107}Sn [107Sn] have a J^{π} [J pi] = $5/2^{+}$ ground state and a J^{π} [J pi]= $7/2^{+}$ first excited state at 200 keV and 151 keV respectively. The exclusive cross sections for one-neutron knockout from ^{106}Sn [106Sn] and ^{108}Sn [108Sn] show that the ground state are dominated by the $d_{5/2}$ [d5/2] single-particle state.

Table of Contents

List of Tables

List of Figures

Chapter 1

Introduction

The region around doubly-magic ^{100}Sn is a rich area of study for testing nuclear models. Measuring the properties of these nuclei provides insight into shell structure in the region. In addition to the N=Z=50 closed shells, these nuclei also have a close proximity to the proton drip-line. In fact, ^{100}Sn is the heaviest N=Z doubly magic nucleus bound against ground state proton decay.

The ^{100}Sn region is also important to astrophysical calculations. The rapid proton capture process (rp process) proceeds along the tin isotopic chain, via a series of β decays and proton captures, from ^{99}Sn to ^{105}Sn. This process ends in the SnSbTe cycle shown in Fig 1.1. The properties of nuclei involved in the rp process are vital to the understanding of X-ray bursts and the synthesis of proton-rich nuclei.

Recent experiments have lead to conflicting assignments of the single-particle states in ^{101}Sn. Previous to this study, the lightest odd-mass tin nucleus with a firm spin-parity assignment was ^{109}Sn. The experiment discussed here not only provides insight into the spin-parity assignments of light odd-mass tin isotopes, but also helps determine the degree of configuration mixing present in the ground state of the even-mass isotopes ^{108,106}Sn. Measurements probing the nature of ground states in the light tin region are crucial to determining the structure of these nuclei, and for testing theoretical models in this region where experimental data are scarce.

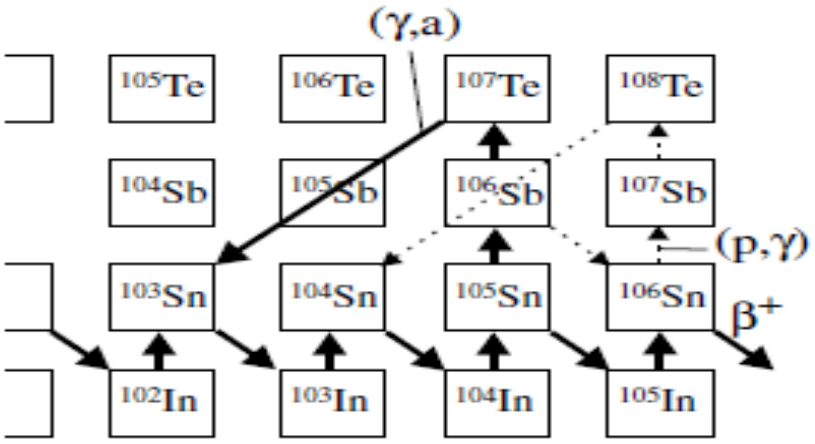

Figure 1.1: The SnSbTe cycle which serves as an end point to the rp process. Figure taken from Schatz et al. (2001)

1.1 Previous experimental studies on light tins

Many of the qualities which make the light tin isotopes interesting, also makes them difficult to probe experimentally. Far from stability, production rates via fragmentation decrease due to the increase in the number of neutrons which must be removed while preserving the proton number. In addition to fragmentation, fusion evaporation reactions and α-decay techniques have been used to study this region.

The first observation of ^{100}Sn was reported in 1994 by Schneider et al. (1994). A beryllium target was bombarded with a ^{124}Xe beam at GSI using the heavy-ion synchroton SIS. The products were then separated using the fragment separator FRS and in-flight isotope identification was performed using magnetic rigidity, time of flight, and energy measurements. After 277 hours of beam time, seven ^{100}Sn nuclei were detected. Shortly after, ^{100}Sn was also identified at GANIL using a stable ^{112}Sn beam and a natural ^{58}Ni target. Approximately five nuclei were detected per day Lewitowicz et al. (1994).

Half-lives, decay spectra, cross sections, and excited-state energy levels have been probed by experiments on light tin isotopes. The interpretation of two experiments

have lead to conflicting assignments of the single-particle states in ^{101}Sn although there is no conflict in the data themselves. Examining these experiments provides insight into the causes of the conflict and how a spin-parity assignment for ^{107}Sn and ^{105}Sn can help.

1.1.1 Overview of ^{46}Ti(^{58}Ni,3n)^{101}Sn experiment

At the Argonne Tandem-Linac Accelerator System (ATLAS) facility of Argonne National Laboratory, a ^{46}Ti(^{58}Ni,3n)^{101}Sn reaction was used to produce ^{101}Sn nuclei. The Gammasphere germanium-detector array was used to detect in-beam γ rays. The reaction products were separated by the Fragment Mass Analyzer and sent to a Parallel Grid Avalanche Counter (PGAC)-ionization chamber (IC) combination. The PGAC was used to provide a measurement of position and the IC measured the energy loss of the fragments. Mass slits were used to accept recoils with a mass of A=101 and 23^+ and 24^+ charge states. These recoils were implanted into a Double-sided Silicon Strip Detector (DSSD) where the β-decays were observed. Silicon (Si) detectors surrounding the DSSD detected β particles escaping through the front of the DSSD.

The recoil-decay tagging (RDT) method was used to correlate prompt γ-rays associated with the production of ^{101}Sn with β-delayed protons from the decay of ^{101}Sn. In order to isolate γ rays associated with ^{101}Sn, decay events were required to have a decay time less than 5 s, deposit an energy in the DSSD between 1 and 5 MeV, and be coincident with a β particle in the surrounding Si detectors or scattered between two neighboring strips in the DSSD. In the resulting γ ray spectrum, shown in Fig 1.2, peaks are clearly visible at 172 and 248 keV. For comparison, γ-rays randomly correlated with β particles are shown in panel b of Fig 1.2. The 248 keV peak present in both spectra is associated with the decay of ^{101}Ag which was a beam contaminant produced after the evaporation of 3 protons. Protons gated on the

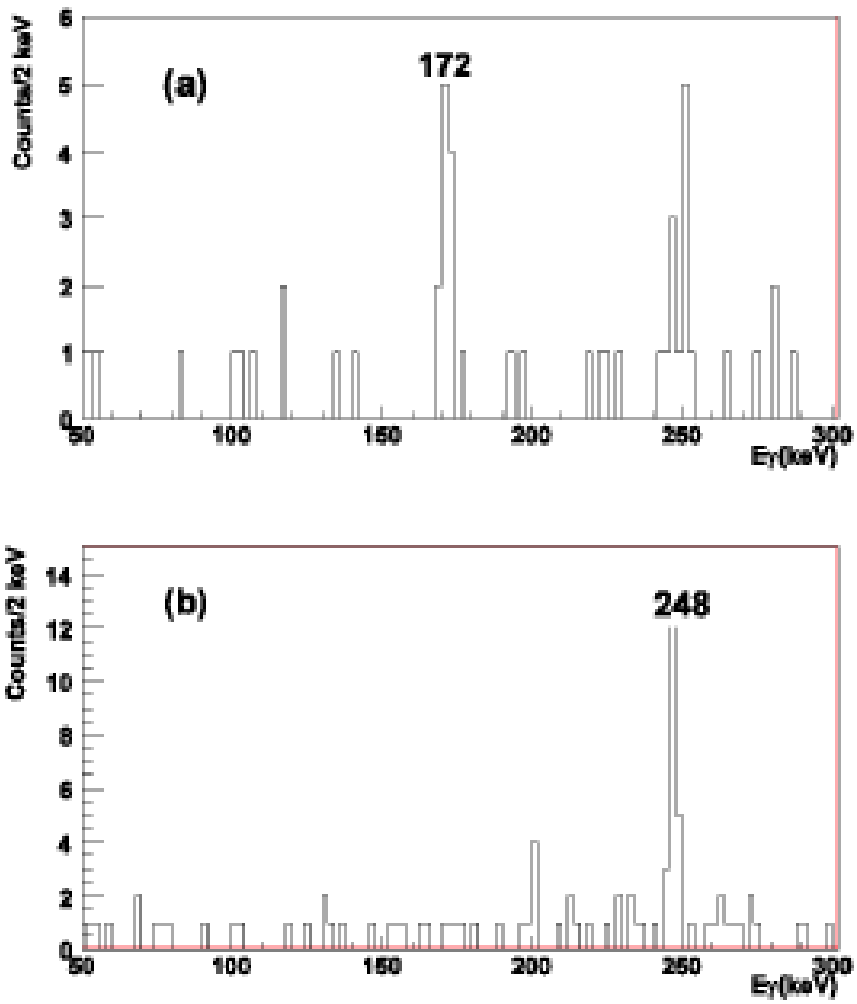

Figure 1.2: Spectra from the ^{46}Ti(^{58}Ni, 3n)^{101}Sn experiment (a)γ rays correlated with decays which have decay times of less than 5 s, an energy between 1.5 and 4.5 MeV, and coincident with betas or scattering between neighboring DSSD strips. (b) γ rays correlated with β decays from outside the 5 s window. Seweryniak et al. (2007)

172 keV γ rays had a decay time consistent with the half-life of ^{101}Sn obtained from previous measurements. The 172 keV γ-ray was therefore interpreted as the transition from an excited state to the ground state in ^{101}Sn.

The $g_{7/2}$ - $d_{5/2}$ energy gap in the N=51 isotones decreases from 2.2 MeV in ^{91}Zr to 441 keV in ^{99}Cd. A linear extrapolation of this energy gap leads to the assumption of the ^{101}Sn $g_{7/2}$ state being 190 keV above the $d_{5/2}$ ground state. As a result, the 172 keV γ-ray was interpreted as the transition from a $g_{7/2}$ excited state to the $d_{5/2}$

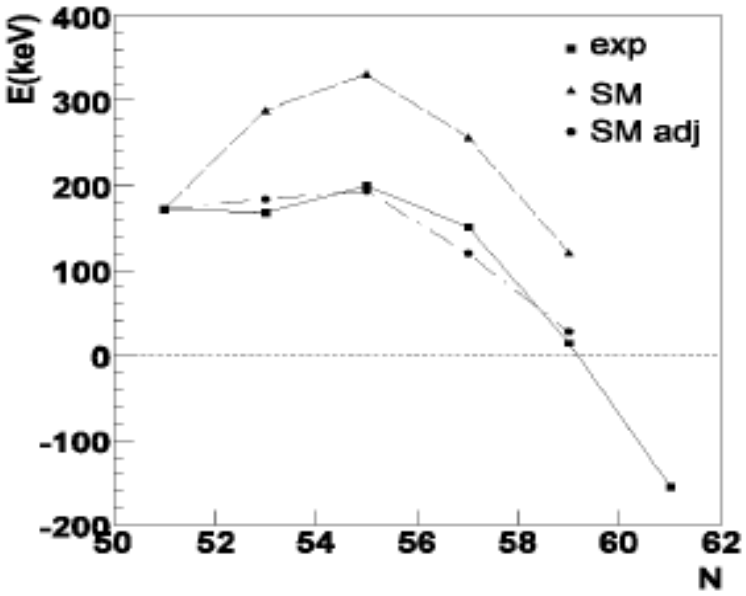

Figure 1.3: The energy splitting between the $7/2^+$ and the $5/2^+$ states, obtained via shell-model calculations, for light tin nuclei. The squares represent measured excitation energies, triangles represent shell model calculations obtained using matrix elements from Hjorth-Jensen et al. (1995). The circles represent the same shell model calculations performed with the $(g_{7/2})^2_{0+}$ matrix element reduced by 30% Seweryniak et al. (2007)

.

ground state. The energies of multi-particle configurations were calculated, using the shell model, to support this interpretation. The calculations yield an energy difference between the two states that is about 200 keV too large but has a pattern similar to experimental data. As shown in Fig 1.3, a reduction of about 30% in the $(g_{7/2})^2_{0+}$ matrix element provides better agreement with experimental data Seweryniak et al. (2007).

1.1.2 Overview of Alpha Decay of ^{109}Xe$\rightarrow^{105}$Te$\rightarrow^{101}$Sn experiments

At the Holifield Radioactive Ion Beam Facility (HRIBF) of Oak Ridge National Laboratory, the two lowest states of ^{101}Sn were observed via the double-alpha decay

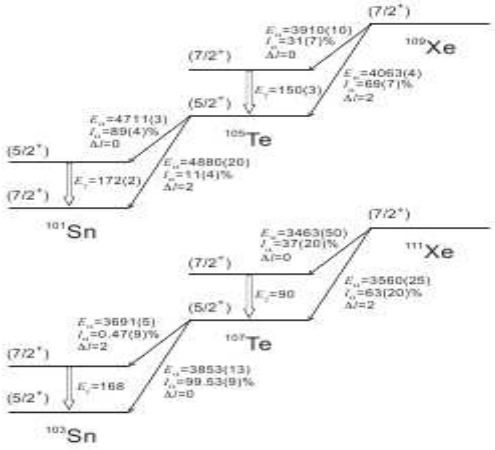

Figure 1.4: Proposed ^{109}Xe→^{105}Te→^{101}Sn α decay chain. Figure from Darby et al. (2010) produced with results for ^{103}Sn chain from Schardt et al. (1979), Sewerniak et al. (2002), and Fahlander et al. (2001).

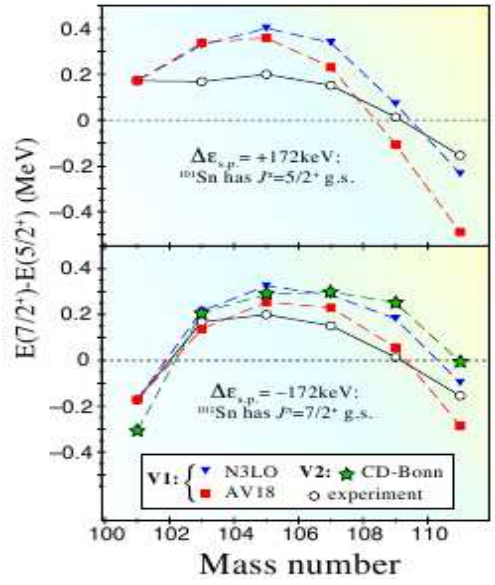

Figure 1.5: The energy splitting between the $7/2^+$ and the $5/2^+$ states. Figure from Darby et al. (2010).

of ^{109}Xe in two experiments Darby et al. (2010). The A = 109 fusion evaporation products of ^{54}Fe and ^{58}Ni were resolved by mass to charge ratio and separated from the unreacted primary beam using the recoil mass spectrometer (RMS). At the focal plane of the RMS, the fusion evaporation residues were implanted into a double-sided

silicon strip detector (DSSD) and the α decay chain ^{109}Xe$\rightarrow^{105}$Te$\rightarrow^{101}$Sn was studied. In the second experiment, the setup was augmented with High Purity Germanium (HPGe) clover detectors, placed around the DSSD, for γ-ray detection. This allowed for the detection of α-γ coincidences.

For the ^{109}Xe$\rightarrow^{105}$Te transition, two α decays of 3910(10) keV and 4063(4) keV were observed. The ^{105}Te$\rightarrow^{101}$Sn transition resulted in two more α decays of 4711(3) keV and 4880(20) keV. The first three decays are consistent with values from previous experiments. The final α decay was previously unknown. The differences in the energy of the alpha decays result in excitation energies of 153(11) keV and 170(20) keV, for the first excited states in ^{105}Te and ^{101}Sn, respectively. The 170 keV is consistent with the excitation energy measured in the ATLAS experiment discussed in Section 1.1.1.

In the HPGe detector experiment, γ rays were observed at 150(3) keV and 172(2) keV. These values are comparable to the excitation energies calculated from the alpha decays and represent the depopulation of the first excited states in ^{105}Te and ^{101}Sn. After taking the intensities of each transition into account, the decay scheme illustrated at the top of Fig 1.4 was proposed. Interpretation of the proposed decay scheme within the standard model of α decay led to the conclusion that the ground state spins of ^{105}Te and ^{101}Sn differ from each other, while the spin of the ground state of ^{105}Te is equal to the spin of first excited state of ^{101}Sn. Comparison with the proposed decay scheme of neighboring ^{111}Xe$\rightarrow^{107}$Te$\rightarrow^{103}$Sn, shown at the bottom of Fig 1.4 , reveals an unexpected level inversion occurring between ^{101}Sn and ^{103}Sn.

Shell model calculations using realistic interactions as described in Hjorth-Jensen et al. (1995) were used to lend further support to the interpretation of the experimental results. These calculations were performed using a ^{100}Sn core, with residual interactions based on AV18 Wiringa et al. (1995) or N3LO Entem and Machleidt (2003) nucleon-nucleon potentials, and a ^{88}Sr core, with residual

interactions derived from the CD-Bonn potential Machleidt (2001). The calculations were performed with the $g_{7/2}$ single particle state below the $d_{5/2}$ and with the $d_{5/2}$ single particle state below the $g_{7/2}$ then the results were compared to experimental data, as shown in Fig 1.5. The results obtained assuming the $g_{7/2}$ level is below the $d_{5/2}$ level, naturally leading to a $7/2^+$ ground state for ^{101}Sn, agree with experiment much better than those assuming a lower $d_{5/2}$ level, which does not accurately reproduce the trend in the $g_{7/2}$-$d_{5/2}$ splitting over the ^{103}Sn to ^{111}Sn isotopes. Both scenarios result in a $5/2^+$ ground state for ^{103}Sn and predict the change from a $5/2^+$ to $7/2^+$ ground state occurring from ^{109}Sn to ^{111}Sn Darby et al. (2010).

1.1.3 Experimental Conclusions

Although the conclusions drawn from the two experiments conflict, the data are not incompatible. The observation of a 172 keV γ ray in the ^{109}Xe decay chain Darby et al. (2010) reaffirms the excited state energy obtained from the ^{46}Ti(^{58}Ni,3n)^{101}Sn reaction Seweryniak et al. (2007). Furthermore, the results obtained from the ATLAS experiment do not exclude the possibility of a $7/2^+$ ground state. Instead, it was the extrapolation from heavier tin nuclei, and of the $g_{7/2}$ - $d_{5/2}$ energy gap in N=51 isotones, as well as the absence of higher energy γ rays that lead to the $5/2^+$ ground state assignment. As noted in Darby et al. (2010), it is also possible that the level inversion seen in the ^{109}Xe decay chain could occur between the ^{109}Xe and ^{105}Te, although no evidence is seen.

Calculations using realistic interactions, as prescribed by Hjorth-Jensen et al. (1995), predict highly mixed ground states for the even mass light tins. As seen in Fig 1.6, the $g_{7/2}$ configuration is calculated to dominate the ^{102}Sn and ^{104}Sn isotopes while the $d_{5/2}$ configuration dominates the ^{106}Sn and ^{108}Sn isotopes. In contrast, the surface delta interaction (SDI) calculations predict that all light tin nuclei will have

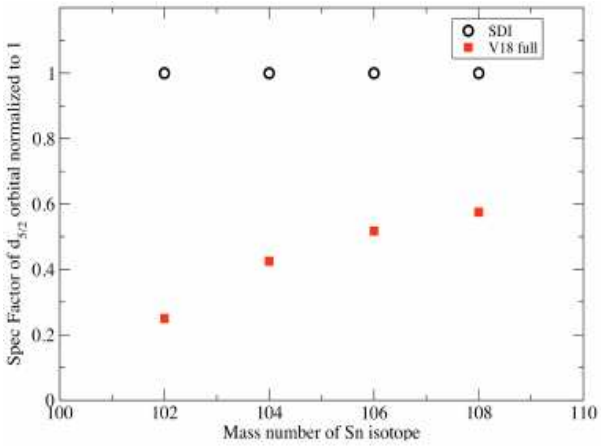

Figure 1.6: The neutron $d_{5/2}$ ground state spectroscopic factors normalized to 1. Calculated using SDI and V18 interactions.

neutron occupations of 100% for the $d_{5/2}$ state. Additional spectroscopic data will make it possible to resolve the controversy.

1.2 Scope

The goals of this study are to measure ℓ-values of the valence neutrons in ^{108}Sn and ^{106}Sn via a one neutron knockout reaction. The momentum distribution of the resulting residue is dependent on the ℓ-value of the removed neutron. Coincident γ-rays were measured such that knockout to excited states could be separated from knockout to the ground state. By being able to separate these knockout channels, it is possible to characterize the odd-mass residue in terms of a hole in the d- or g- orbital with respect to the ground state of the even-mass beam nucleus. This differentiates between the possible $5/2^+$ and $7/2^+$ ground states of the odd-mass residues. The ℓ-values for the nuclei are determined from the measured momentum distributions and cross sections are extracted for each knockout channel. The ratios of the cross sections for each knockout channel probe the degree of configuration mixing of the $(d_{5/2})^N$ and $(g_{7/2})^N$ neutron states for the ^{108}Sn and ^{106}Sn nuclei.

Chapter 2

Theoretical Considerations

In this work we use a direct nuclear reaction to study the structure of nuclei above the doubly-magic ^{100}Sn. Therefore, we need to discuss nuclear shell model origin of magic numbers as well as the direct reaction theory user for moementum distribution calculations.

2.1 Nuclear Shell Model

The nuclear shell model describes the structure of the atomic nucleus in an analogous way to how the atomic shell model describes the electron configuration of an atom. In the atomic shell model, the electron shells are filled in order of increasing energy in a manner consistent with the Pauli principle, which states that identical fermions can not occupy the same quantum state. This creates a core of filled shells and an outer shell which may be partially occupied by any remaining valence electrons. Atomic properties are determined primarily by these valence electrons and change smoothly within a shell but drastically between them.

A similar pattern of smoothly changing properties followed by abrupt discontinuities is seen in nuclei, leading to the concept of a nuclear shell model. The total number of nucleons required to completely fill a shell is known as a magic number.

The experimental evidence supporting the existence of nuclear shells includes: proton and neutron separation energies, increased abundance of nuclei with a N or Z magic number, and a larger excitation energy for the first excited state of magic nuclei compared to those in the surrounding region. Experimentally, the magic numbers have been determined for stable nuclei to be: 2, 8, 20, 28, 50, 82, 126 (for neutrons).

In this model, it is assumed that each nucleon moves in a central potential well created by the nucleon-nucleon interactions of the other A-1 nucleons. Therefore, the model uses a one-body Hamiltonian of the form:

$$h(r) = -\frac{\hbar^2}{2\mu}\nabla^2 + v(r) \tag{2.1}$$

where μ is the reduced mass of the nucleon.

The potential is commonly estimated using the three-dimensional harmonic oscillator potential:

$$v(r) = \frac{1}{2}\mu\omega_o^2 r^2 \tag{2.2}$$

where ω_o is the frequency. All states in each shell, N, are degenerate with energy:

$$\varepsilon_N = (N + \frac{3}{2})\hbar\omega_o. \tag{2.3}$$

The maximum number of nucleons that a harmonic oscillator shell can hold is given by:

$$D_N = 2\sum(2\ell + 1) = (N + 1)(N + 2). \tag{2.4}$$

Accordingly, the total number of nucleons that can be accommodated within a maximum shell, N_{max}, is:

$$D_{max} = \sum_{N=0}^{N_{max}} D_N = \frac{1}{3}(N_{Max} + 1)(N_{Max} + 2)(N_{Max} + 3). \tag{2.5}$$

Solving for N_{Max} = 0, 1, 2,... gives values for D_{max} = 2, 8, 20, 40, 70, 112. This successfully reproduces the first three magic numbers but not the later ones Wong (1998).

As explained by Mayer and Jensen (1955), accurately reproducing the magic numbers can be accomplished by adding a spin-orbit interaction to the central potential. The spin-orbit interaction is dependent upon the intrinsic spin, s and orbital angular momentum, ℓ, of a nucleon. Leading to the single-particle Hamiltonian:

$$h(r) = -\frac{\hbar^2}{2\mu}\nabla^2 + \frac{1}{2}\mu\omega_o^2 r^2 + as\cdot\ell + b\ell^2 \tag{2.6}$$

where a is a parameter representing the strength of the spin-orbit term and may depend on the nucleon number and the ℓ^2 is required to lower the centroid energy of states with large ℓ-values. Developing this new Hamiltonian in a similar way to the Hamiltonian associated with the three-dimensional harmonic oscillator results in the magic numbers: 2, 8, 20, 28, 50, 82, 126. Thus, the addition of a spin-orbit interaction to the three dimensional harmonic oscillator potential successfully reproduces the magic numbers which were determined experimentally for stable nuclei. The effect that the spin-orbit interaction has on the splitting of the degeneracy can be seen in Fig 2.1.

As discussed in Sec 1.1.2, Darby et al. (2010) used shell model calculations with ^{100}Sn (Z=N=50) and ^{88}Sr (N=50) cores. Both calculations had N=50 closed neutron core with valence neutrons in the $d_{5/2}$, $g_{7/2}$, $d_{3/2}$, $s_{1/2}$, and $h_{11/2}$ orbitals. Their results support the interpretation of a $7/2^+$ ground state for ^{101}Sn. The shell model calculations by Darby et al. (2010) also predict highly mixed ground states for the even-mass neutron deficient tin isotopes with the valence neutrons occupying the $d_{5/2}$ and $g_{7/2}$ orbitals. The degree of mixing in ^{108}Sn and ^{106}Sn has been probed in this work and is discussed in Sec 6.2.

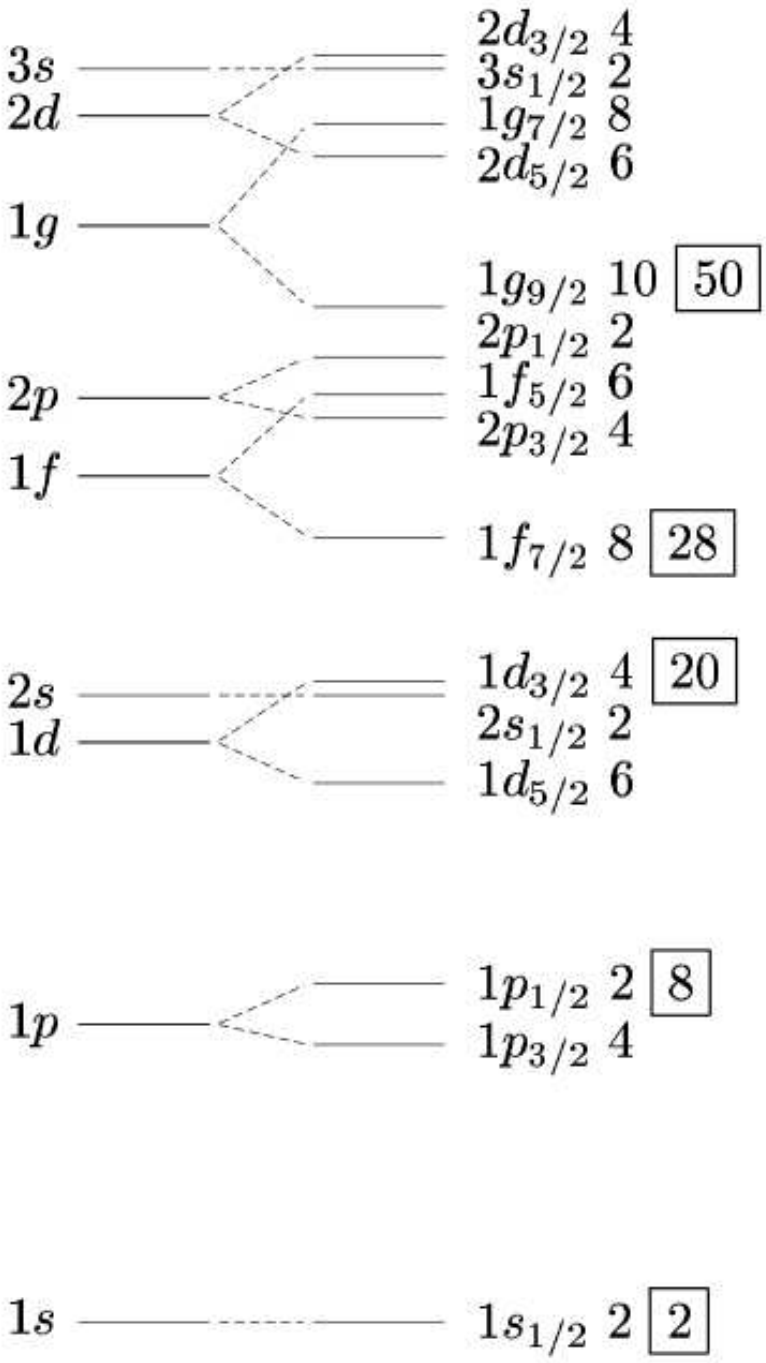

Figure 2.1: The nuclear shell model with magic numbers. The orbital angular momentum ℓ is denoted on the left. The degeneracy splitting resulting from adding the spin-orbit term to the potential is indicated on the right. The magic numbers on the far right are the total number of nucleons required for a closed shell. Figure from Padgett (2011).

2.2 Spectator Core Eikonal Reaction Model

The reaction used in this study was modeled using the Spectator Core Eikonal Reaction Model. The Spectator Core Eikonal model assumes that there are pre-formed components in the ground state wave function. The reaction is treated as a three-body problem comprised of a target, nucleon, and core. This greatly reduces the complexity over dealing with the 108 nucleons in the projectile and 9 in the target. The core, the knockout residue (as opposed to the ^{100}Sn core of the shell model), is a spectator and is only permited in the calculation to interact elastically with the target Hussein and McVoy (1985).

The cross section for populating a core state c is:

$$\sigma(c) = \sum C^2S(c, n\ell j)\sigma_{sp}(S_n, n\ell j) \tag{2.7}$$

where n, l, and j are their respective quantum numbers, C^2S is the spectroscopic factor for the removal of a nucleon with those quantum numbers, S_n is the nucleon separation energy, and σ_{sp} is the single particle cross section from the stripping and diffraction mechanism such that $\sigma_{sp} = \sigma_{sp}^{str} + \sigma_{sp}^{diff}$ Tostevin (2001). The reaction model is discussed in detail in Tostevin (2001) and is based on the sudden and Eikonal approximations. The sudden approximation assumes that the projectile is at a high enough kinetic energy and the interaction time between the projectile and target is assumed to be short such that the probability of a multi-step process is negligible. Thus, the relative motion of the residue and removed nucleon can be ignored. The Eikonal approximation assumes that the deflection of the projectile due to the interaction with the target is also negligible. Therefore, the trajectory of the projectile can be taken to be a straight line. The momentum distributions are calculated from the differential cross sections via a black-disc approximation as in Hansen (1996), which reduces the 3D nucleus to a 2D 100% absorptive disc. Any

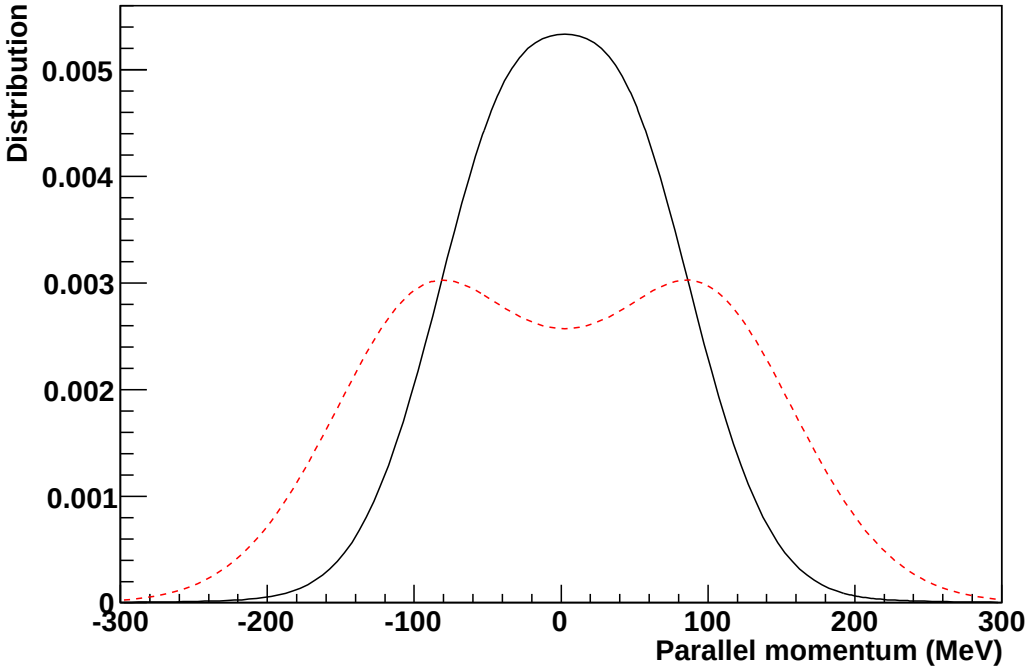

Figure 2.2: Calculated parallel momentum distributions for ^{107}Sn. Black solid line is the momentum distribution for a $\ell = 2$ state and red solid line is a $\ell = 4$ state. Calculations courtesy of Jeff Tostevin.Tostevin (2013)

nucleon incident on disc is assumed to be absorbed. The calculated momentum distribution for ^{107}Sn is shown in Fig 2.2. Here, the black line is the momentum distribution for removing a $d_{5/2}$ neutron from a ^{108}Sn core and the red line is the distribution for removing a $g_{7/2}$ neutron from a ^{108}Sn core. In Chapter 6, these calculated momentum distributions are compared to the momentum distributions obtained experimentally to make spin-pairity assignments.

Chapter 3

Experimental Approach

The one-neutron knockout reactions ^{9}Be(^{108}Sn, ^{107}Sn + γ)n and ^{9}Be(^{106}Sn, ^{105}Sn + γ)n were performed at the National Superconducting Cyclotron Laboratory (NSCL) in February 2011. One-neutron knockout reactions are powerful spectroscopic tools even at low beam rate, down to a few particles per second.

A primary beam of ^{124}Xe was accelerated in the coupled cyclotron to 140 MeV/nucleon before being fragmented on a ^{9}Be target. The reaction products were separated using the A1900 fragment separator, which produced the required ^{108}Sn and ^{106}Sn secondary beams. These beams were directed to a ^{9}Be target in the target chamber of the S800. The reaction products were identified and their momentum distributions measured using the S800. The γ-ray detector array CAESAR was used to measure the γ-rays that were in coincidence with the knockout reaction. This chapter will describe the primary and secondary beams, the one neutron knockout, and the equipment used for the experiment.

3.1 Neutron Knockout

A one-neutron knockout reaction has been used for this work to measure the orbital angular momentum (ℓ-value) so that spin-parity assignments can be made of the

resulting reaction residue. A nucleon knockout reaction occurs when a projectile nucleus makes a peripheral collision with a target nucleus. The collision results in one or two nucleons being removed from the projectile in a direct reaction with no intermediate state. The longitudinal, or parallel, momentum distribution of the knockout residue is dependent upon the orbital angular momentum of the knocked out nucleon. The ℓ-value of the removed nucleon is deduced from the shape of the longitudinal momentum distribution. Performing γ-ray spectroscopy in coincidence with a knockout reaction makes it possible to disinguish knockout to the ground state of the residue from knockout to an excited state. Spectroscopic factors can be extracted by measuring the cross sections of knockout to the individual states.

Experimental momentum distributions are compared with reaction calculations (Sec 2.2 and Fig 2.2) in order to determine the ℓ-value of the removed nucleon. The beam energies used for the neutron knockout experiment described here are high enough that eikonal and sudden approximation theoretical framework can be applied Gade and Glasmacher (2008). For this work, a spectator core eikonal model is used to caclulate the momentum distributions Tostevin (2001).

3.2 Primary Beam Production

A stable primary ion beam of $^{124}Xe^{48+}$ was provided at 140 MeV/nucleon by the coupled cyclotrons at the NSCL. The first step in preparing a stable primary beam is to obtain ions from a stable material, typically a gas or solid metal. This is accomplished at the NSCL in an electron cyclotron resonance (ECR) ion source. The stable gas is injected into the ECR ion source, if the source material is solid then it is first heated in an oven. Once in the ECR, the gas is bombarded by electrons. The electrons collide with and ionize the atoms. After this initial ionization, the gas is injected into the K500 cyclotron.

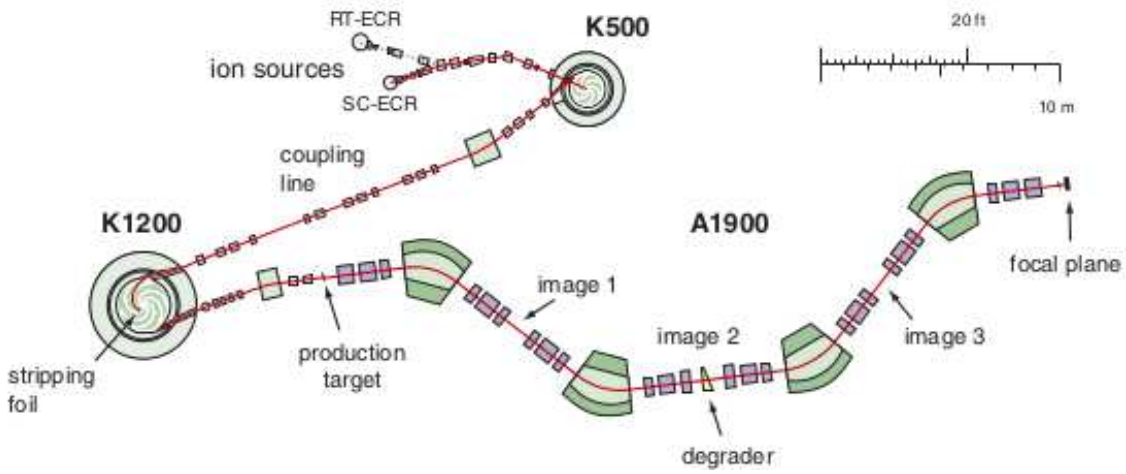

Figure 3.1: A schematic of the Coupled Cyclotron Facility and the A1900 fragment separator at the NSCL. The beam path is shown in red from the ion source to the A1900 focal plane. Figure is from Stolz et al. (2005).

The K500 cyclotron serves as the injector cyclotron for the coupled system. The K500 accelerates the beam to an energy of 12.27 MeV/nucleon before injecting it into the K1200 (see Fig 3.2). In order to further ionize the beam, a carbon stripper foil is placed in the middle of the K1200. The beam exits the K1200 cyclotron as a $^{124}Xe^{48+}$ 140 MeV/nucleon beam at an intensity of 10 pnA. The cyclotrons accomplish the beam acceleration by constraining the beam to a circular path within the cyclotron using a magnetic field. Each cyclotron has three sets of "dees" and "hills" with a strong RF field applied across the gap. As the beam passes over these gaps it is accelerated by the field. The accelertion increases the gyroradius ρ of the beam such that:

$$\rho = \frac{p}{qB} = \frac{\gamma m v}{qB} \tag{3.1}$$

where γ, m, v, and q are the Lorentz factor, mass, velocity, and charge of the particles and B is the strength of the magnetic field see Stolz et al. (2005) for example.

3.3 Secondary Beam Selection

Radioactive ions are produced from the primary beam fragmentation as it impinges on a thick ^{9}Be production target. Some of the primary beam collides with the nuclei in the production target, this collision breaks the beam nucleus and produces exotic isotopes moving at approximately the same veolocity as the projectile. Immediately following the production target is the A1900 fragment separator, shown in Fig 3.2.

The A1900 fragment separator is composed of four dipole magnets and eight quadrupole triplets. The magnets have a maximum magnetic rigidity of 6 Tm Stolz et al. (2005). Dipole magnets are dispersive, separating isotopes based on magnetic rigidity, and are used to bend the beam. Quadrupole magnets are used to focus the beam. A single quadrupole magnet can focus the beam in only one direction and defocuses it in the perpendicular direction. Therefore, a doublet is required to focus the beam in both directions. Using a quadrupole triplet provides an additional degree of freedom and allows for better performance than can be achieved with a doublet. The magnetic field of the dipoles can be tuned to separate isotopes by their mass-to-charge ratio but eq. 3.1 shows that a magnetic field cannot separate isotopes with a different charge but the same mass-to-charge ratio and velocity.

To achieve unambiguous particle selection, a degrader is located at image 2, the mid-acceptance position of the A1900. The degrader is a piece of aluminum that the beam passes through. The isotopes slow down roughly proportional to Z^2/v^2, resulting in a different velocity for isotopes with a different Z. This change in velocity allows for the remaining dipole magnets to separate nuclei with the same mass-to-charge ratio but different Z. Since each isotope has a small velocity spread and the energy loss in the wedge is inversely proportional to v^2, the result of passing through a uniformly thick degrader would be to increase the velocity spread of an isotope. Therefore, the degrader is wedge shaped, so that faster particles will pass through

more of the degrader than the slower particles. The shape of the wedge is matched to the dispersion of a selected isotope. The result is that all particles of a given isotope will have the same velocity change Baumann (2011).

The effect a magnetic field has on a charged particle is dependent upon the magnetic rigidity of the particle. As a result, beam particles are dispersed by the A1900 magnetic dipoles based on their mass-to-charge ratio. Particles with a larger mass-to-charge ratio experience a longer flight path through the A1900. Therefore, the time of flight measurement can be used to distinguish between isotopes of different magnetic rigidity. A thin plastic scintillator is located at the end of the A1900. During beam development, this scintillator provides a time measurement that is used to calculate the time of flight. This time of flight, along with an energy loss measurement, allows for the unambiguous identification of the secondary beam. During the experiment, the time measurement from this scintillator is used to calculate the time of flight for reaction products (discussed in detail in Sec 3.5.3).

3.4 The S800 Spectrograph

The S800 Spectrograph is a high acceptance, high resolution spectrograph. As shown in Fig 3.2, there are two segments of the S800: the analysis line, which includes a plastic scintillator and the intermediate image detectors, and the spectrograph.

The analysis line of the S800 is used to characterize the incoming beam and tune it to the reaction target. The analysis line begins at the object box and ends at the target. It has two modes of operation: focused and dispersion matching mode. For this experiment, the analysis line was operated in dispersion matching mode where the analysis line is tuned so that the momentum spread of the beam at the object is cancelled at the focal plane. As a result, the beam is momentum dispersed on the target at about 10cm/%. The momentum dispersion on the target limits the

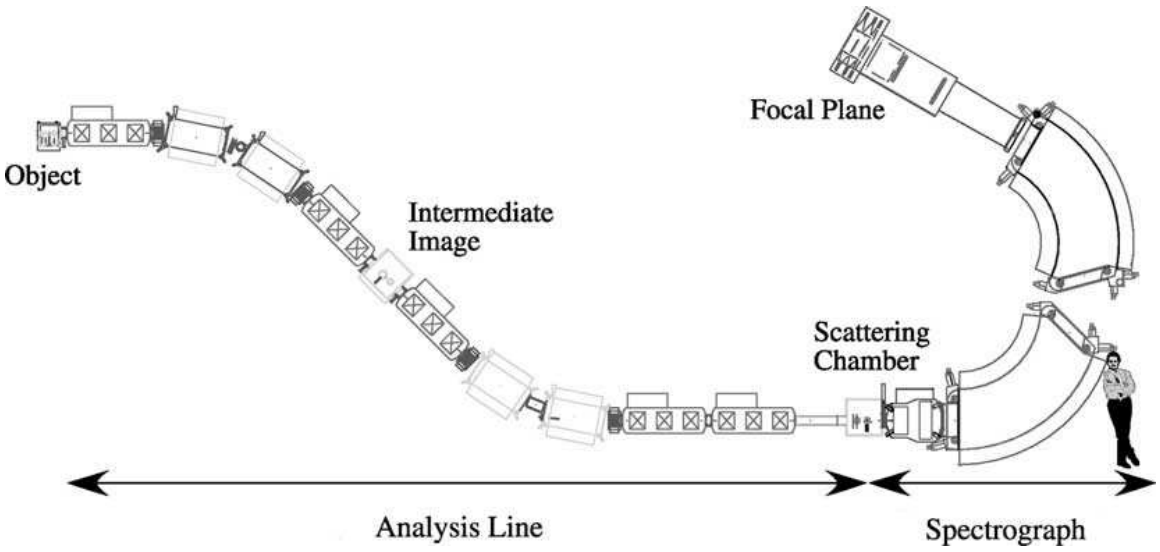

Figure 3.2: A schematic of the S800 Spectrograph. Figure is from Bazin et al. (1993).

maximum momentum acceptance of the analysis line. The momentum acceptance is generally limted to ±0.25% to accommodate 2" targets Bazin (2012). This mode of operation does not require measuring the momentum of incoming particles prior to the reaction, resulting in the maximum energy resolution of the S800.

Although not used for this work, the S800 can also be operated in focused mode where the analysis line is tuned so that the beam is focused at the target and the momentum spread of the beam is not cancelled at the focal plane. Since the beam is focused at the target, it allows for the largest momentum acceptance of ±2% in the analysis line Bazin (2012). Since the momentum spread of the beam is not canceled at the focal plane, this mode requires the momentum of incoming particles to be measured prior to the reaction. The detectors used for tracking the incoming particles are two Parallel Plate Avalanche Counters (PPAC) with individual strip readouts. These detectors were not required for this work and will not be discussed in detail.

The incoming beam from the A1900 is focused at the object position, Fig 3.2, where there is a thin plastic scintillator, discussed in detail in Sec 3.5.3. The beam

is then directed through the analysis line to the target chamber. Here, the high efficiency CsI(Na) scintillator array, CAESAR, was used for detecting the γ-rays resulting from the decay of reaction products and will be discussed in detail in Sec 3.6. A 47 mg/cm^2 thick ^{9}Be target was placed at the target position of the S800. The spectrograph portion of the S800 follows the target. The spectrograph consists of two dipole magnets and a quadrupole doublet. The dipole magnets disperse the beam according to its mass-to-charge ratio and the quadrupole doublet refocuses the beam in the x and y direction, similar to the A1900 described in Sec 3.3. The magnets are tuned so that they guide the desired reaction products to the focal plane. The momentum acceptance of the spectrograph is $\pm 3\%$ and it has a maximum rigidity of 4 Tm Bazin et al. (1993). The S800 terminates with the focal plane where an array of detectors provide information on the charge, position, and time-of-flight of reaction products.

3.5 S800 Focal Plane

The S800 focal plane, Fig 3.3, is the end point of the S800 where the charge, position, energy, and time-of-flight of transmitted ions are measured. The reaction products will first pass through two Cathode Readout Drift Chambers (CRDCs), followed by an ionization chamber, a thin plastic scintillator, and finally end in a hodoscope. The following sections will discuss these detectors in detail with the exception of the hodoscope. In order to achieve suitable particle identification, the pressure in the ionization chamber was increased so that the reaction products were slowed to such a degree that they rarely penetrated more than a few segments of the hodoscope. Consequently, the hodoscope was not used in the data analysis.

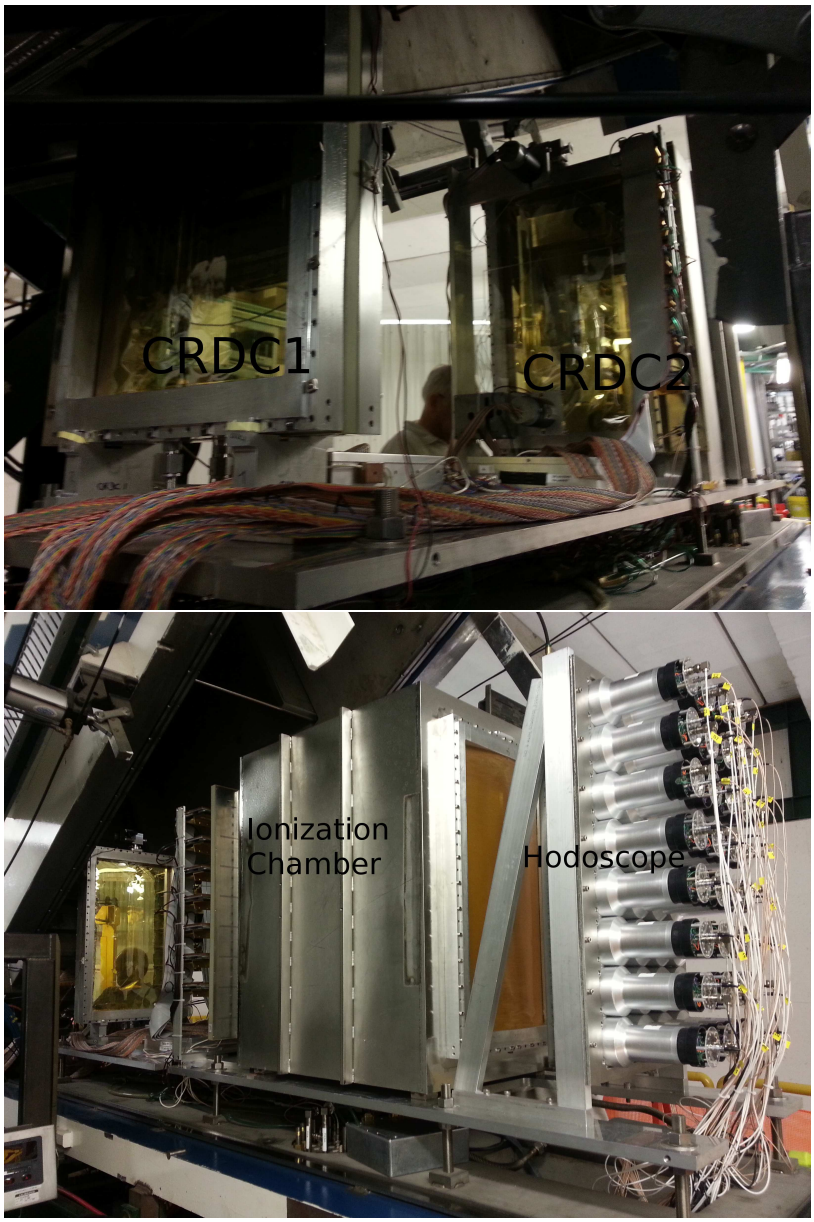

Figure 3.3: A rare look at the S800 Focal Plane. The CRDCs, ionization chamber, and hodoscope are labeled and clearly visible. The E1 scintillator is used as the exit window for the ionization chamber.

3.5.1 Cathode Readout Drift Counters

Upon entering the S800 focal plane, the beam particles travel through a pair of Cathode Readout Drift Counters (CRDC) separated by approximately 1 m. Individually, each CRDC determines particle position in the S800 disperive (x) and

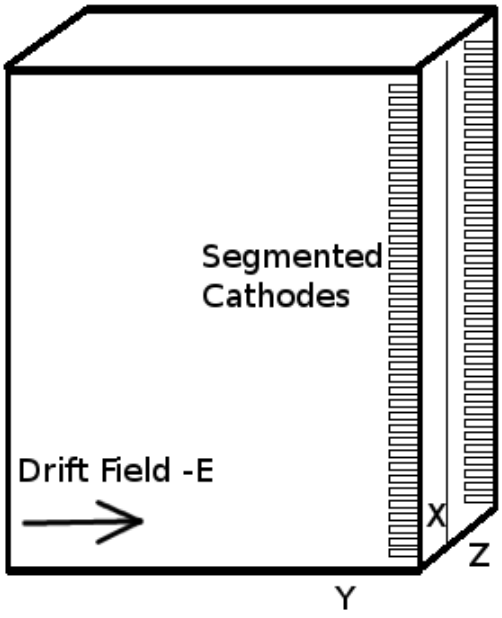

Figure 3.4: Schematic of a CRDC in the focal plane of the S800. The x (dispersive), y (non-dispersive), and z (beam direction) labeled. The x and y positions of the interaction are determined using the segmented cathode and the anode respectively.

non-dispersive (y) directions. The detectors are 56 cm in the x direction by 26 cm in the y direction and have a position resolution of .5 mm in both directions Bazin (2012). These position measurements make it possible to reconstruct the trajectory on an event-by-event basis back to the target position. The method for reconstructing trajectories will be discussed in detail in Sec 5.3, where the calculation of momentum distributions is covered.

The CRDCs are primarily composed of a drift chamber filled with a 80% CF_4 (carbon tetrafluoride) and 20% C_4H_10 (isobutane) gas mixture, an anode wire, and a cathode segmented into 224 pads, each 2.54 mm wide Bazin (2012). The drift chamber has a negative bias voltage applied in the y-direction and the anode wire is at positive voltage. As the positively charged beam particles pass through the drift chamber they ionize the gas, creating free electrons. These electrons drift through

the gas towards the positvely charged anode wire. The drift time of the electrons is used to calculate the y position of the interaction between the beam particles and the CRDC gas mixture. This drift time is determined using the difference of timing signals from the E1 scintillator, discussed in 3.5.3, and the anode wire. As the electrons drift towards the anode, image charges are induced on the cathode. The centroid of the image charges are calculated and the pad position best matching the centroid is used as the x position of the interaction. Drift times can take up to 20 μs, therefore, the CRDCs can run at rates up to 5000 particles per second.

Changes in temperature and pressure can cause the electron drift time to vary throughout the experiment. In order to determine the drift times, a tungsten mask with holes in known positions is inserted in front of each CRDC periodically throughout the experiment. These masks runs are used to calibrate the x and y positioning of the CRDCs, as described in 4.3.

3.5.2 Ionization Chamber

Following the CRDC detectors, the beam particles pass through an ionization chamber. The S800 ionization chamber was upgraded shortly before the start of this experiment and is composed of 16 anode and cathode pairs aligned perpendicular to the beam path and is operational at pressures of up to 600 Torr Bazin (2012). For this work, the chamber was filled with P10 gas (90% argon and 10% methane) at a pressure of 450 Torr. The ionization chamber functions similar to the CRDCs described in 3.5.1. As the positively charged isotopes pass through the chamber they ionize the gas creating free electrons and positively charged gas ions. The free electrons drift to the nearest anode while the gas ions drift to the nearest cathode. The amount of gas ionized by a particle represents the energy loss of that particle, as given by the Bethe formula:

$$\frac{dE}{dx} = \frac{4\pi}{m_e c^2} \cdot \frac{nz^2}{\beta^2} \cdot \left(\frac{e^2}{4\pi\varepsilon_0}\right)^2 \cdot \left[\ln\left(\frac{2m_e c^2\beta^2}{I \cdot (1-\beta^2)}\right) - \beta^2\right]. \tag{3.2}$$

where c is the speed of light, ε_0 the vacuum permittivity, β is v/c, e the electron charge, m_e the electron rest mass, and n is the electron density of the gas. The energy loss in the ionization chamber is dominated by charge of the particle squared. Therefore, by measuring the energy loss in the ionization chamber it is possible to distinguish between particles with different charges.

3.5.3 Time of Flight and Trigger Scintillator

The exit window of the ionization chamber is a large area thin plastic scintillator with photomultiplier tubes located at the top and bottom of the scintillator Bazin (2012). This scintillator is known as the e1 scintillator and is used primarily for timing information and as the trigger for the S800. Aside from timing signals, the scintillator can also provide energy signals. The ratio of the top energy signal to the bottom energy signal can be used to provide a x position (the dispersive direction) measurement.

The timing scintillator signal is measured against either the scintillator located at the end of the A1900, known as the x focal plane (xfp) scintillator, or the one located at the beginning of the S800, known as the object (obj) scintillator. The difference of the e1 and the obj/xfp timing signals provides a measure of the time-of-flight of a particle. As discussed in Sec 3.3, the effect a magnetic field has on a charged particle is dependent upon the magnetic rigidity of the particle. As a result, beam particle are dispersed by the S800 magnetic dipoles such that particles with a larger mass-to-charge ratio experience a longer flight path through the S800. Therefore, the time-of-flight measurement can be used to distinguish between isotopes of different magnetic rigidity.

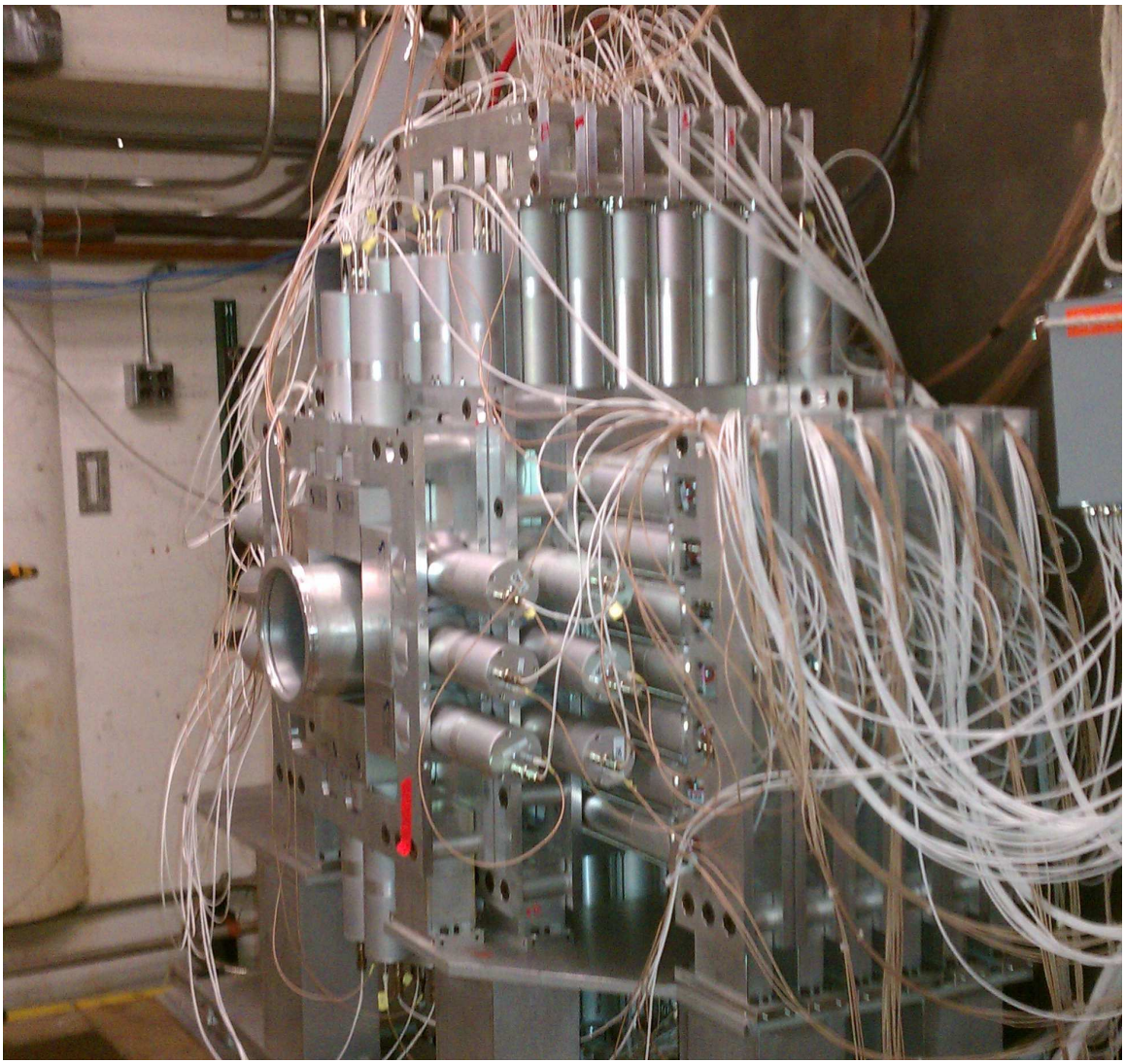

Figure 3.5: Photo of CAESAR in position around the target chamber of the S800.

3.6 Gamma Ray Detector

The in-beam γ-ray spectroscopy was performed using the high-efficiency Caesium-iodide scintillator array (CAESAR). CAESAR is composed of 192 CsI(Na) scintillation crystals arranged in a ring formation, as shown in Fig 3.5, labeled A to J as shown in Fig 3.6. The crystals making up the array come in two different sizes. The 44 larger crystals have a 3x3 inch face and are 3 inches long and are located in rings A(10), B(14), I(14), and J(10). The smaller crystals have a 2x2 inch face and are 4

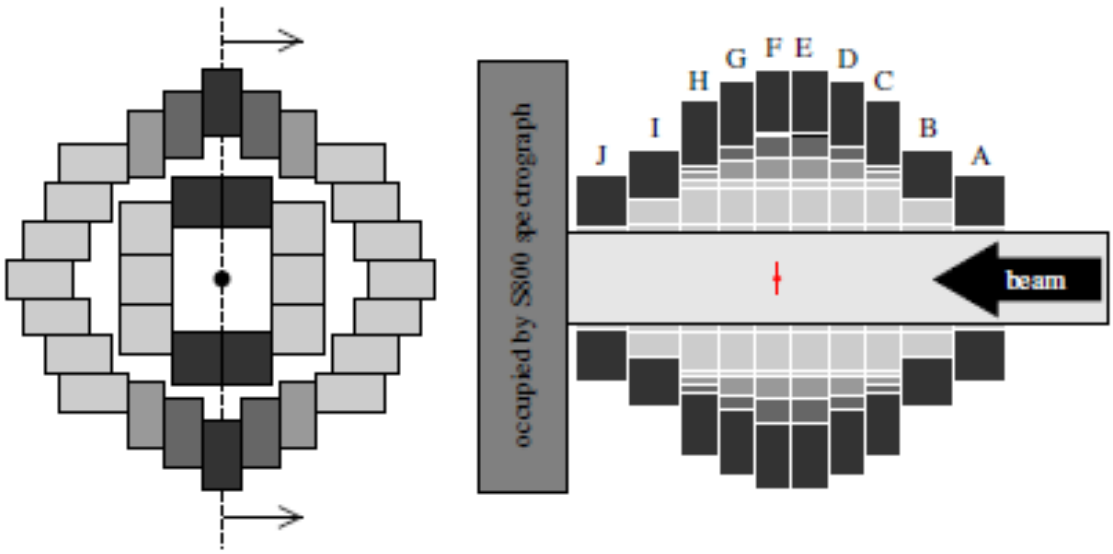

Figure 3.6: Left: Cross-sectional view of J and F perpendicular to the beam axis. Right: Cross-sectional view of all 10 rings parallel to the beam axis. Figure from Weisshaar et al. (2010)

inches long. Rings C through H are composed of these crystals with 24 of them in each ring Weisshaar et al. (2010).

There are three separate types of interactions that a γ-ray can have with a detector material. For this work, the primary γ-rays of interest are under 200 keV and their main interaction channel with the detector is through the photoelectric effect. When this interaction occurs, the γ-ray is completely absorbed by an atom in the detector which emits an electron. Other possible interaction channels are Compton scattering and pair production. In Compton scattering, a γ-ray interacts with an electron in the detection material depositing energy into the electron and scattering the γ-ray. The scattered γ-ray may interact again with the same crystal or pass into a neighboring detector. For γ-rays with energies in excess of 1.022 MeV, twice the mass-energy of the electron, it is possible for the γ-ray to interact with a nucleus of the detector material which absorbs part of the γ-ray energy and emits an electron-positron pair.

The kinetic energy of the pair is:

$$KE = E_\gamma - 2m_e c^2. \tag{3.3}$$

When the positron collides with an eletron both particles are annihilated and two γ-rays are emmited, each at an energy of 511 MeV.

3.6.1 Nearest Neighbor Addback

Although the photoelectric effect deposits the full energy of the photon into a single detector, Compton scattering and pair production interactions typically only partially deposit the γ-ray energy into a single detector. Often, the γ-ray from a Compton scattering interaction is scattered into a neighboring detector. Since random coincidence in two neighboring detectors is unlikely, whenever neighboring detectors simultaneously register events it is valid to assume that a single γ-ray was the cause.

A common method known as, nearest neighbor addback, has been implemented to reconstruct the original γ-ray energy. For each event, the analysis code checks to see if neighboring detectors had signals. Whenever this occurs, the energies are summed together and the detector with the highest energy is used for Doppler reconstruction, Sec 3.6.2. This method helps to increase the efficiency of CAESAR significantly at energies greater than 1 MeV and can also help to improve the signal to background ratio at lower energies.

3.6.2 Doppler Correction

When the source of a γ-ray is moving at relativistic speeds, the energy measured in the lab frame will be Doppler shifted. These energies must be Doppler corrected into the rest frame of the source according to the formula:

$$E_{rest} = E_{lab} \cdot \gamma(1 - \beta \cos\theta) \tag{3.4}$$

where γ is the lorentz factor, β is the ratio of v/c, θ is the angle between the direction of the source and the location where the γ-ray was detected. The value of θ is taken to be the angle between the beam trajectory at the target and the center of the detector in which the γ-ray was detected. The doppler shift varies depending upon the value of $\cos\theta$ with the most extreme shift occuring at the most forward and backward angles (rings A and J). There is some uncertainty in this value since the precise location of the interaction can only be narrowed down to a specific detector. It is not possible to know precisely where in the target the reaction occurred and the velocity of the γ-ray source decreases in the reaction target. Therefore, the velocity used for Doppler correction is the mid-target velocity. These sources of uncertainty result in a broadening of the Doppler corrected energy peak known as Doppler broadening. The Doppler broadening is largest whenever the uncertainty in the position has the largest impact. This occurs at the side angles (rings E and F) where small changes in θ have large impacts on the doppler shift.

Chapter 4

Experimental Calibrations

4.1 Ionization Chamber Calibration

4.1.1 Gain Match

The 16 channels in the ionization chamber each provide an energy loss measurement for a portion of the gas. The total energy lost in the ionization chamber is the sum of the energy lost in each channel:

$$ic_{sum} = \sum_{i=1}^{16} de_i. \tag{4.1}$$

As shown in the uncalibrated spectrum in Fig 4.1, the raw energy loss of each channel differs. Since the total energy loss is the sum of the energy lost in each channel, the channels must have their energy spectra gain matched to one of the channels. This is best accomplished by selecting two isotopes with different charges and calculating the centroid of the energy loss for each isotope in all 16 channels of the ionization chamber. These centroids provide points for determing a linear function to gain match each channel to the selected channel. Fig 4.1 shows the results of using this method to match each channel to the first channel of the ionization chamber.

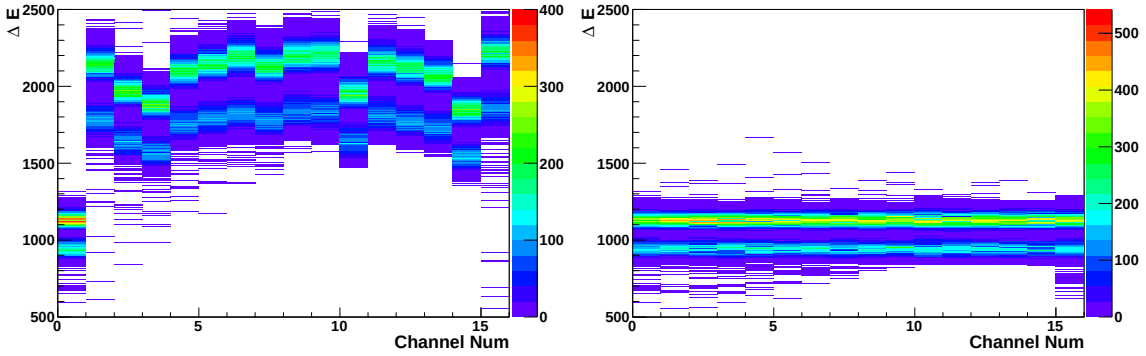

Figure 4.1: The energy loss signal in each ion chamber must be matched. Plots of the uncalibrated (left) and calibrated (right) energy loss measurements are shown for each channel of the ionization chamber for two selected isotopes of the unreacted beam. The channels have been gain matched to the first channel.

4.1.2 Position Correction

In addition to gain matching each segment of the ionization chamber, there is also a small amount of variation in the energy loss signal depending on the position of the particle. Fig 4.2 and Fig 4.3 show the energy lost in the chamber versus the x and y positions measured in the CRDC. Five isotopes have been selected from a vertical line in the particle identification (PID) plot such that each isotope has a different energy loss in the chamber. The energy losses for these isotopes are plotted and the variation with respect to position is obvious. The diagonal slant seen in Fig 4.2 causes particles of an isotope that strike the edge of a CRDC to have the same energy loss as a particle with a different charge striking the opposite edge of the CRDC. There are three parameters used to minmize this energy loss spread and they are applied using:

$$\begin{aligned} dE_0 &= E_{ic} + y_o E_{ic} y \\ dE &= dE_o e^{m x_o x}. \end{aligned} \tag{4.2}$$

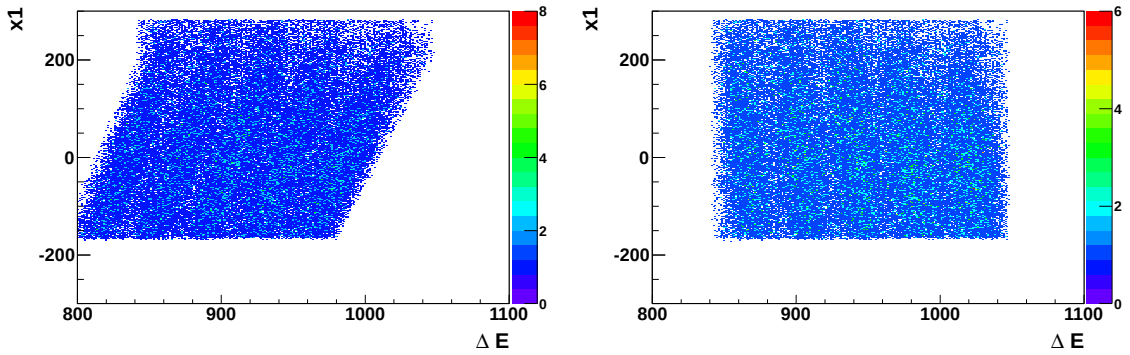

Figure 4.2: The energy loss of five isotopes are plotted with respect to the x (dispersive) position of the particles. The uncalibrated (left) shows that there is a large deviation in the energy loss dependent upon the position. This spread causes the energy loss of the isotopes to overlap. The calibrated (right) shows the result after correcting the energy loss for the position of the particle.

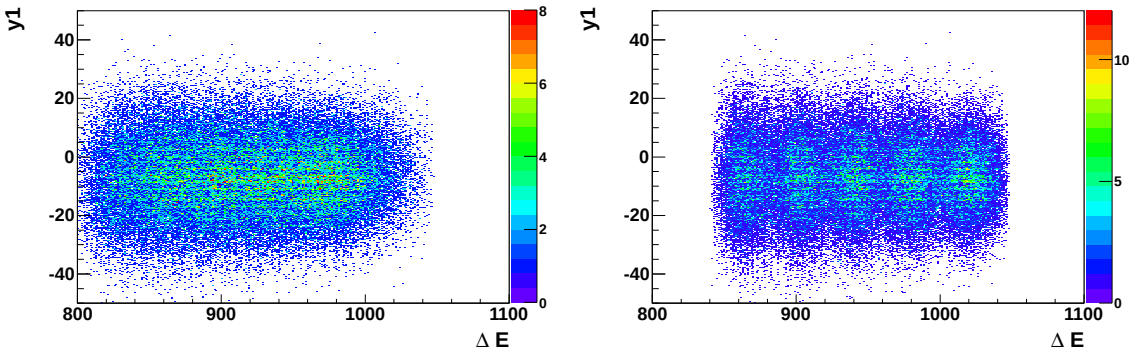

Figure 4.3: The energy loss of five isotopes are plotted with respect to the y (non-dispersive) position of the particles. In the uncalibrated (left) spectrum, the isotopes are not resolved in ΔE. The calibrated (right) spectrum clearly shows each one.

where x and y are the particle x and y position measured in the most upstream CRDC. This correction becomes important for large mass isotopes such as those used in this work. For lighter mass isotopes, the ionization chamber resolution is improved and this correction is less important. For this work, optimal values were required for accurate particle identification. A computer program was written to calculate the parameters that provide the minimum energy spread. The results of these calibrations can be seen in Fig 4.2 and Fig 4.3.

4.2 Time of Flight

As discussed in Sec 3.5.3, plastic scintillators at the end of the A1900 (xfp scintillator) and beginning of the S800 (obj scintillator) are used in conjuction with the large area plastic scintillator that serves as the exit window of the ionization chamber (e1 scintillator) to provide a measurement of the time-of-flight (TOF) of a particle such that isotopes of different magnetic rigidity can be distinguished. The TOF is used in conjunction with the energy loss in the ionization chamber to allow unambiguous particle identification.

It is important for ions of the same isotope to have the smallest TOF variation possible to help avoid overlapping with ions of similar magnetic rigidities. The differences in the energy loss in the target and scattering angle cause particles of the same isotope to take slightly different paths through the S800. This variation in flight path results in an increased TOF spread. The effects of this can be minimized by adjusting the TOF according to the formula:

$$TOF_{corrected} = TOF + m\alpha_{fp} + nx \tag{4.3}$$

where x is the x position of the particle in the most upstream crdc, m and n are fitting parameters, and α_{fp} (AFP) is the angle a particle makes in the dispersive direction with respect to the CRDC (discussed in detail in Sec 5.3). Fig 4.4 and Fig 4.5 show the TOF for neighboring isotopes in the PID plot (discussed in Sec 5.1.2). The TOF has been plotted against the x position and AFP angle respectively. The goal of the calibration is to find values for m and n that minimize the width of the TOF for each isotope so that each can be clearly distinguished in the spectra. The results of this correction can be seen in Fig 4.4 and Fig 4.5. The impact of these corrections and the ones for the ionization chamber discussed in Sec 4.1 on the particle identification can be seen in Fig 4.6.

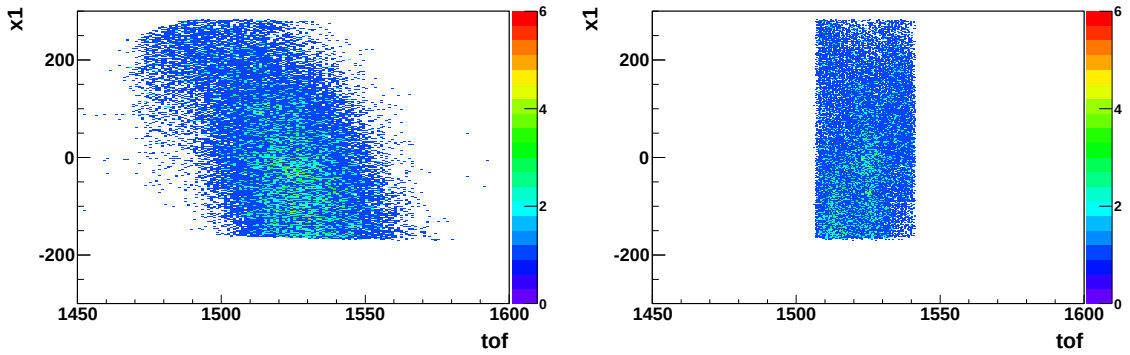

Figure 4.4: The TOF of five isotopes are plotted with respect to the x (dispersive) position of the particles. The uncalibrated (left) shows that there is a large deviation in the TOF dependent upon the position. This spread causes the TOF of the isotopes to overlap. The calibrated (right) shows the result after adjusting the TOF for the position of the particle.

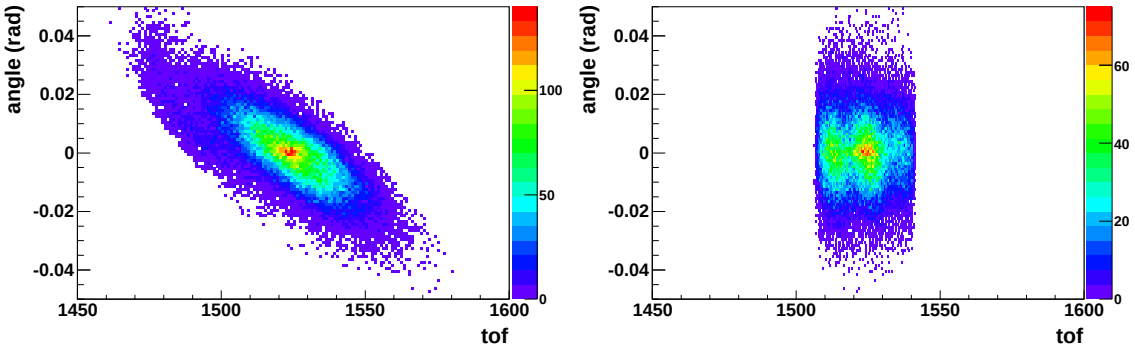

Figure 4.5: The TOF of five isotopes are plotted with respect to their trajectory angle in the dispersive position of the particles. In the uncalibrated (left) spectrum, it is impossible to distinguish between the isotopes. The calibrated (right) spectrum shows them much more clearly.

4.3 Cathode Readout Drift Chamber

4.3.1 Gain Match

The Cathode Readout Drift Chambers (CRDC) provide measurements of the x and y positions. The x position of the particle is taken to be the pad of the segmented cathode associated with the centroid of the image charge produced by the electron

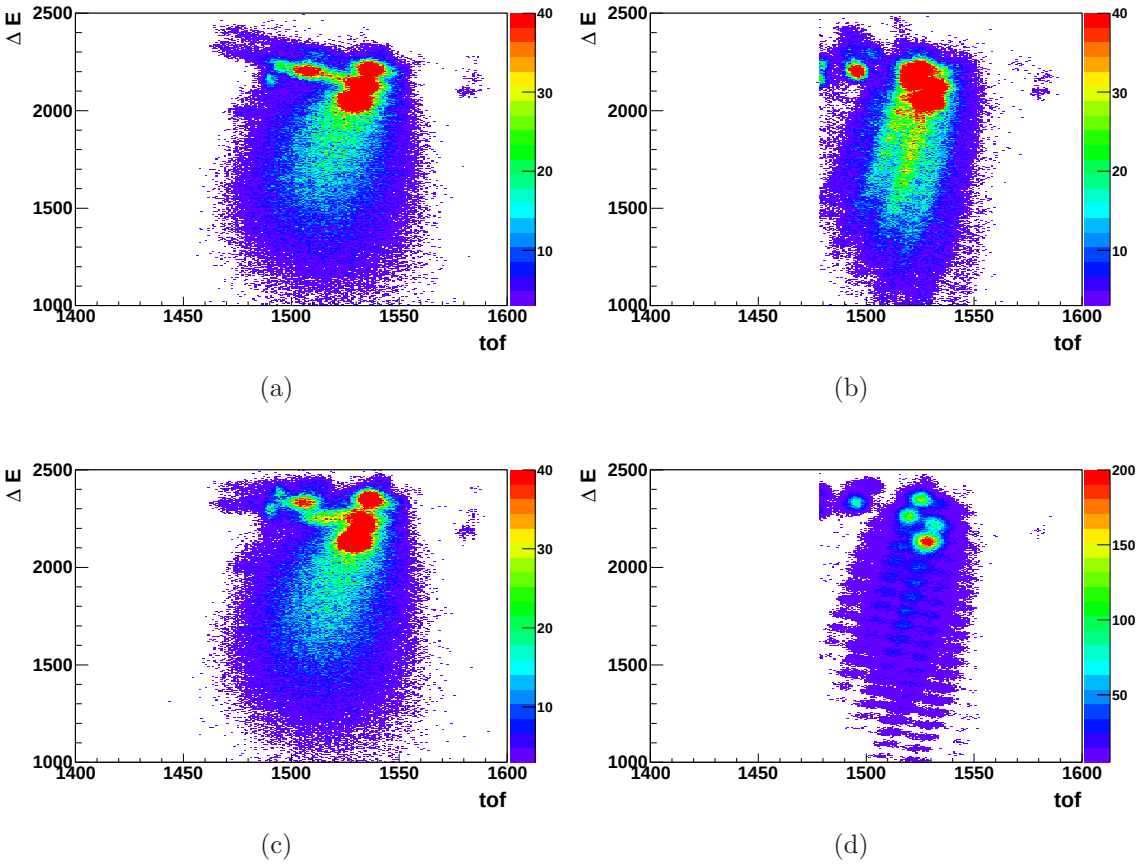

Figure 4.6: The effects of the TOF and energy loss corrections on particle identification are shown. In the uncorrected spectrum (a) it is not resolved between different isotopes. Correcting the TOF (b) and the energy loss measured in the ionization chamber (c) each have a noticeable effect on the PID. Once both corrections are applied (d) the individual fragments are resolved.

drift. In order to properly calculate the centroid, all pads must be gain matched. This is done by gating on unreacted incoming beam ions dispersed across the entire width of the CRDCs. The uncalibrated spectrum in Fig 4.7 shows the rather large difference in the pad readouts. Despite this difference, the uncalibrated data gives reasonable results for the x position of a particle. Neighboring pads all have a similar readout and the image charges all occur in neighboring pads. The centroid is then calculated from these images charges to determine which pad to use as the position of the particle. Since neighboring pads have a similar readout, the resulting centroid is more accurate

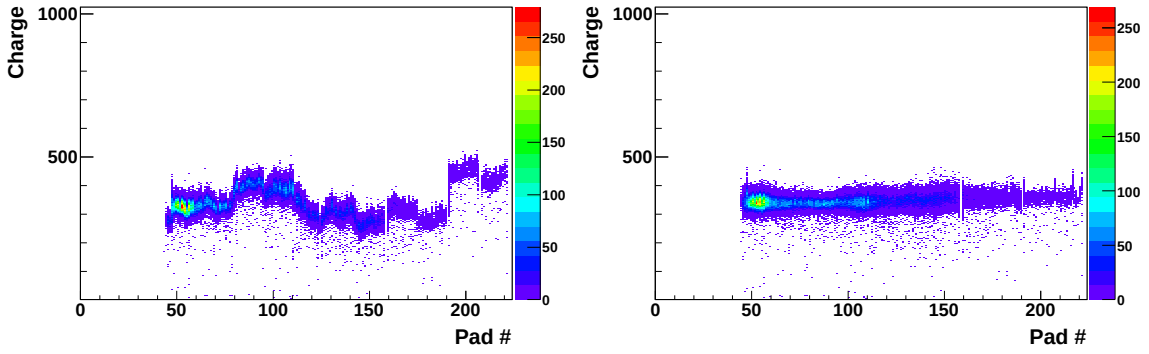

Figure 4.7: The energy deposits into the CRDC pads must be gain matched. Plots of the uncalibrated (left) and calibrated (right) energy deposits are shown for each pad in CRDC1 for a selected isotope.

than Fig 4.7 would suggest. Therefore, this is a second order correction which becomes important when maximum particle position resolution is required. The calibration of the ionization chamber and time-of-flight can be done prior to the gain match of the CRDC despite the fact that their calibration is dependent upon the x position. The calibration is done in a similar way to the gain matching of the ionization chamber (Sec 4.1). One of the 224 pads is chosen as the reference point, and then for each other pad, a slope is calculated to match the readouts to the chosen point. The result of the calibration is shown in Fig 4.7 and the effect that it has on the x position is shown in Fig 4.8

4.3.2 Mask Calibration

The y position in the CRDCs is determined by the drift time of electrons. The drift time is dependent upon the properties of the gas in each CRDC and has been observed to change over time (3.5.1). Therefore, mask calibrations are performed periodically throughout the experiment. These masks have holes in known positions and are inserted directly in front of the CRDC. The mask runs are used to fit the measured y positions to the known y positions in the mask using a linear function.

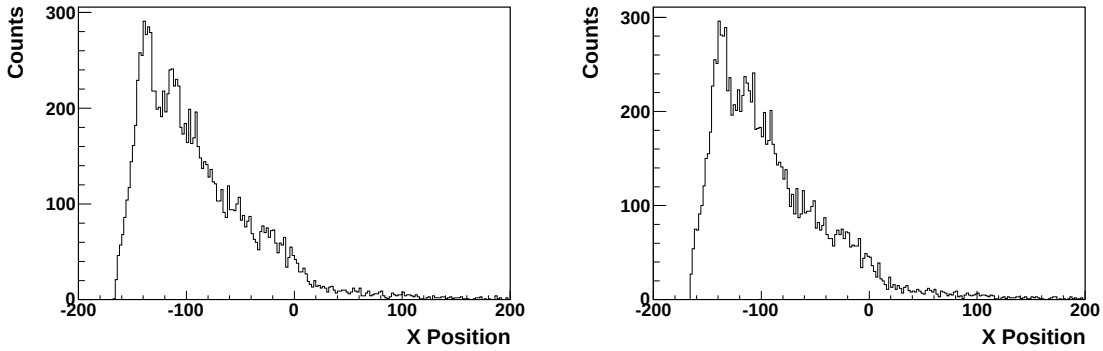

Figure 4.8: The effect of the CRDC pad correction on the x position is shown. The uncalibrated (left) and calibrated (right) spectra are very similar indicating that this correction is of second order.

A spectrum from one of the mask calibrations is shown in Fig 4.9. Furthermore, it is often necessary to examine the y position on a run-by-run basis. This shift can be corrected by adjusting the slope so that the centroid is consistent throughout the experiment (Fig 4.10).

4.4 CAESAR

4.4.1 Energy and Timing Calibrations

Prior to the experiment, each of the crystals of CAESAR were gain matched using a 1836 keV γ ray from an ^{88}Y source. The voltages were set such that the 1836 keV γ ray was around channel 400 in the raw energy spectrum. The energy calibration was performed by measuring the γ ray spectra from a number of calibration sources (^{88}Y, ^{137}Cs, ^{22}Na, ^{60}Co, ^{133}Ba, and ^{57} Co). The sources cover an energy range from about 100 kev to 2 MeV.

For each detector in CAESAR, each source run provides a uncalibrated energy spectrum that is used to map the uncalibrated energies to the known peak energies for that source. This is accomplished by calculating the centroids for each peak in

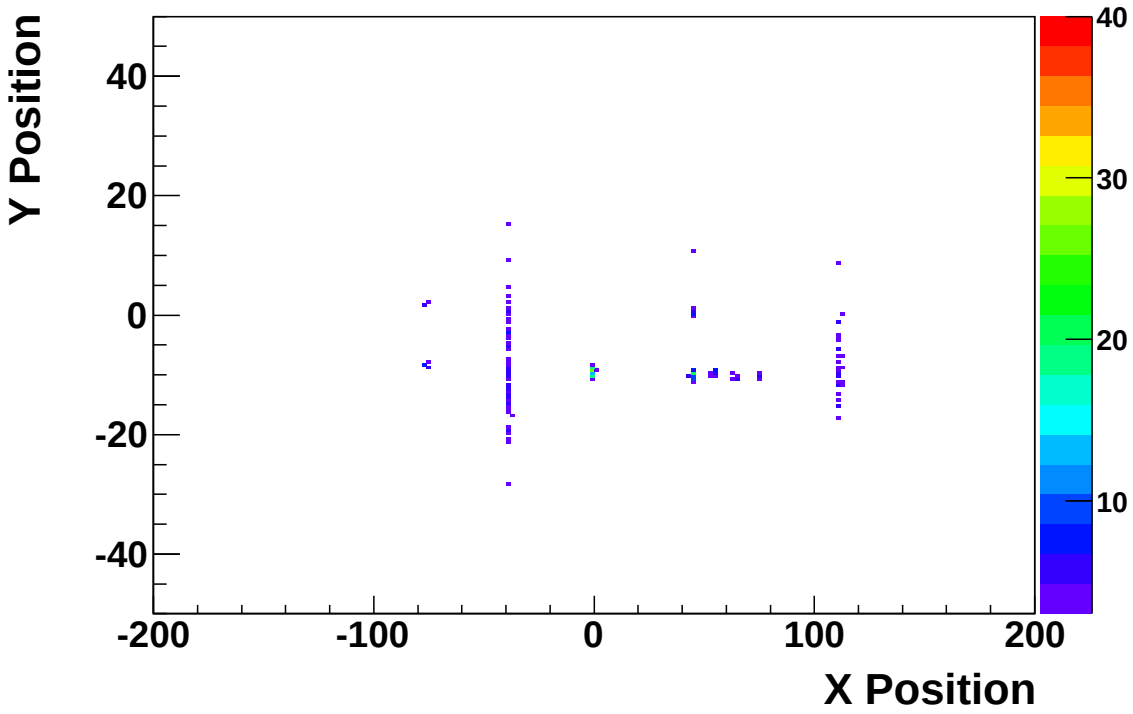

Figure 4.9: The X versus Y positions recorded by the first CRDC are plotted for a mask calibration run. The mask pattern is clearly visible.

multiple source runs. The values of these centroids are then fit to the known values of the γ-ray energies for each peak. For this work, a second order polynomial fit is used so that high energy γ-rays (above 3 MeV) can be examined. It is only at high energies that the non-linearity of the detector crystals can become an issue, a linear fit is adequate for lower energy γ-rays. The resulting energy calibration is shown in Fig 4.11.

In addition to the energy signal, each detector also has a timing signal associated with the event. After calibrating, it is possible to use the timing to reduce the γ ray background by excluding all non-prompt γ rays. The calibration is made in a similar way to the gain matching calibrations performed on the ionization chamber (Sec 4.1) and the CRDCs (Sec 4.3). A detector is chosen to serve as the reference and all the

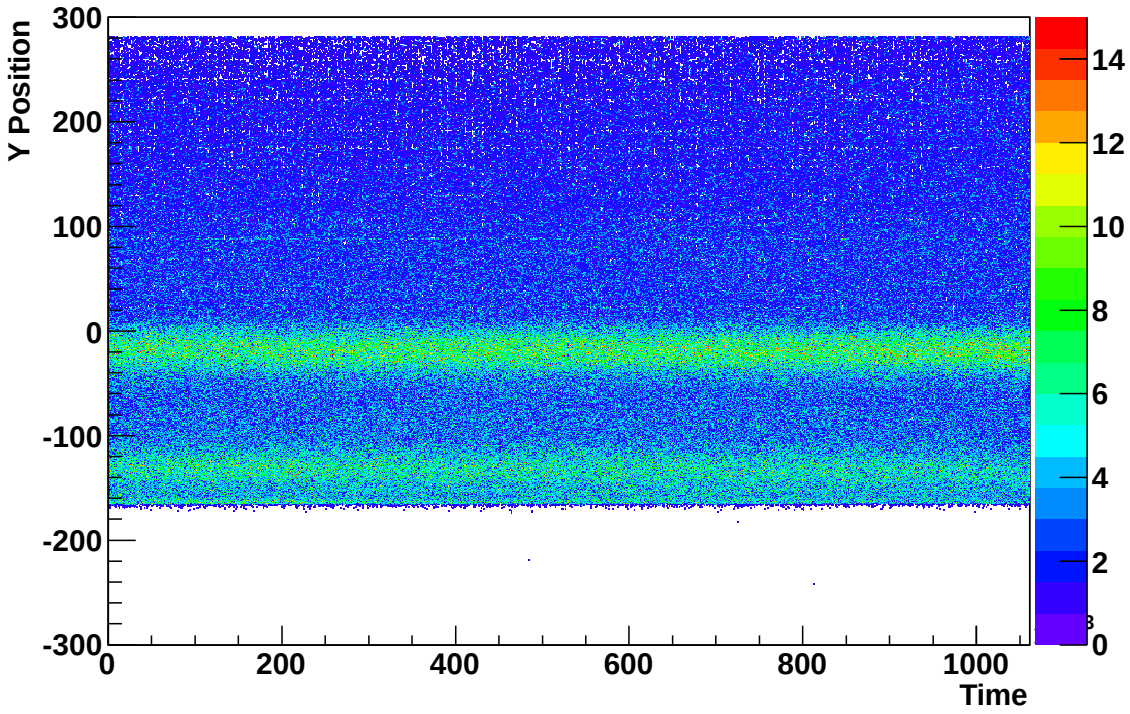

Figure 4.10: The Y position recorded by the first CRDC is shown. For this work, the drift time was consistent throughout the experiment and there was no need to make run-by-run adjustments.

other detectors were matched to it (Fig 4.12). This is best done using one of the source runs that was used for the energy calibration.

4.4.2 Energy Resolution and Efficiency

In order to accurately fit the γ-ray spectra, the resolution of CAESAR must be determined. This is accomplished by fitting a Gaussian distribution to the γ ray spectra from the source runs, as shown in Fig 4.13. The maximum-likelihood estimation (Appendix A) was used to fit the data. The extracted energy resolutions are used as inputs for the GEANT4 simulation (Sec 4.4.3).

Many of the sources used for the energy calibration are calibrated sources which have had their radioactivity measured. The expected number of counts in a peak is

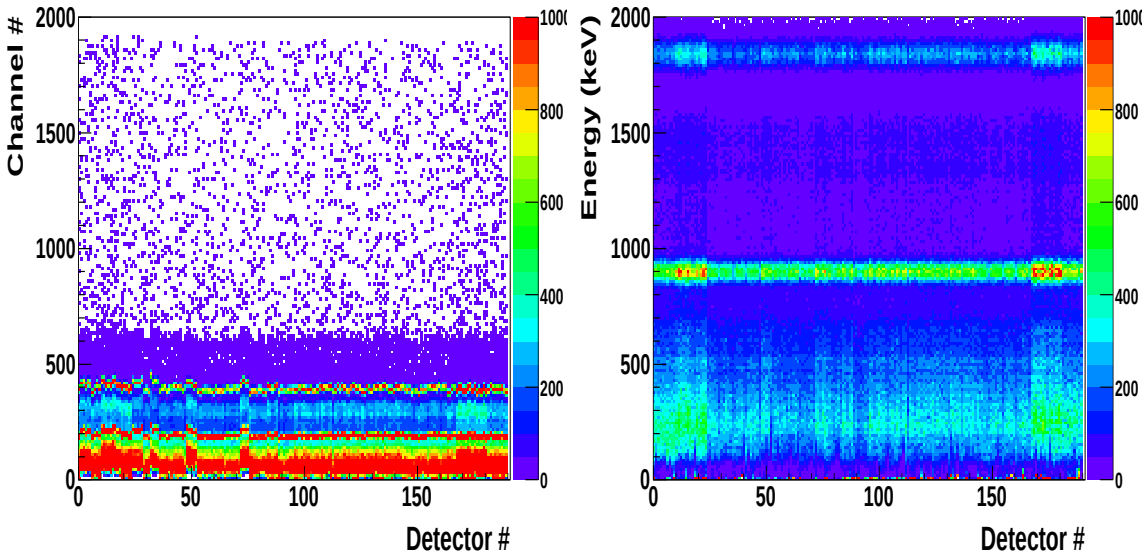

Figure 4.11: (left) Uncalibrated energy plotted as a function of detector numbers. (right) Energy spectrum calibrated using a second order polynomial fit to standard calibration sources. The γ-ray spectra are of a ^{88}Y source run.

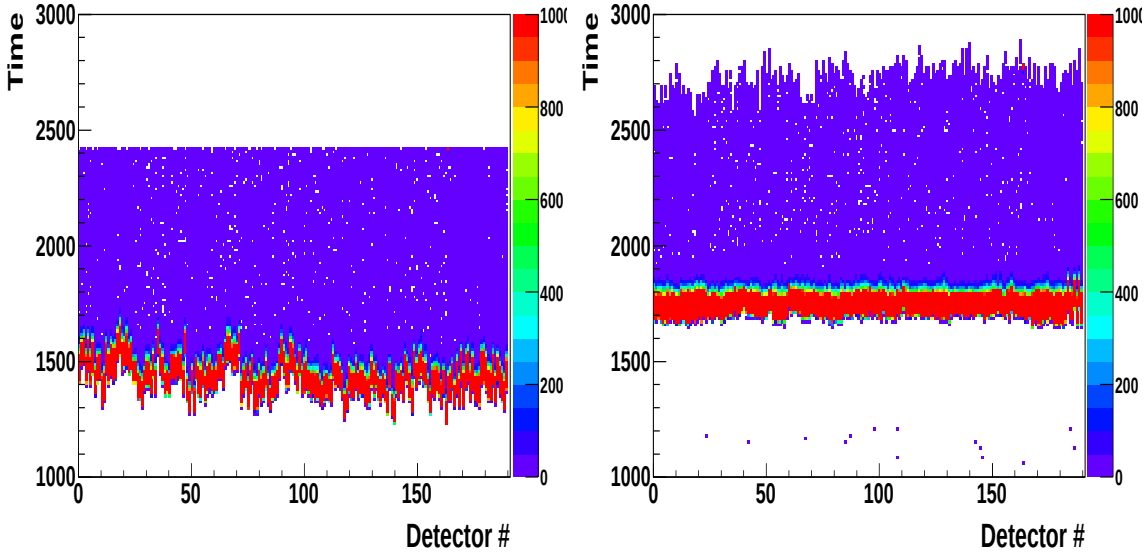

Figure 4.12: (left) Uncalibrated time plotted as a function of detector numbers. (right) Timing spectrum calibrated by shifting the times reported by each detector. The timing spectra are of a ^{88}Y source run.

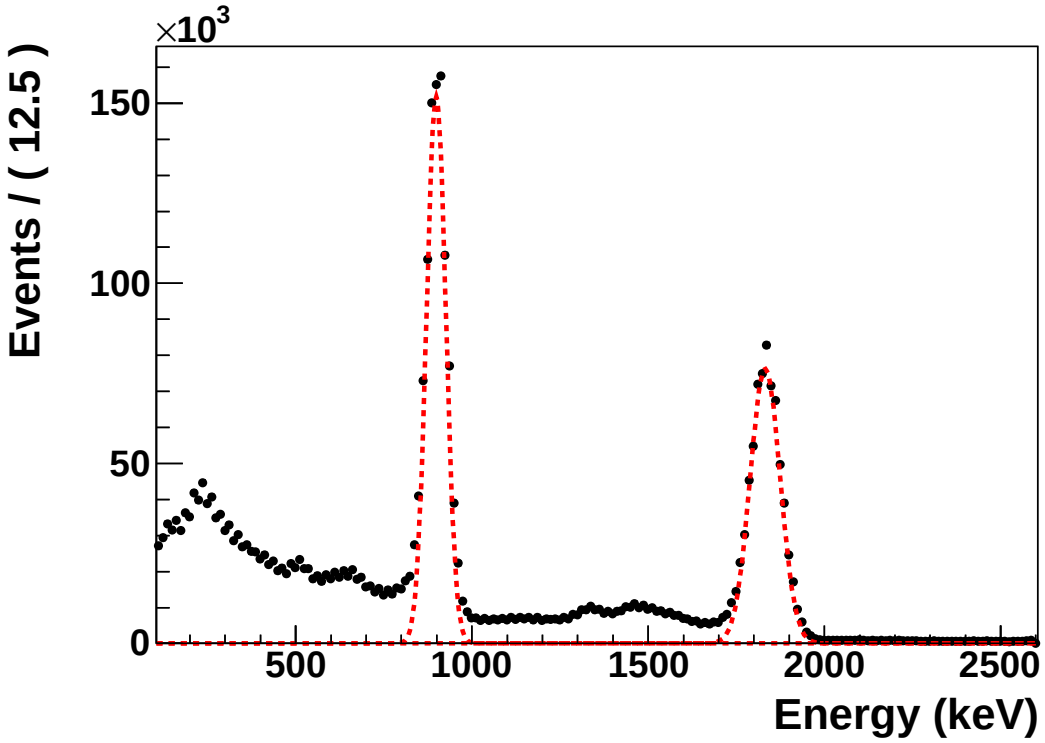

Figure 4.13: The full energy spectrum of a ^{88}Y source run. The spectrum has been fitted using the maximum likelihood estimation method (Appendix A).

calculated. Then the number of counts in the peak area is extrapolated by fitting each spectra with a linear background and using a gaussian the each peak. The ratio of the observed counts to the expected number of counts provides the absolute full-energy peak efficiency for CAESAR at that energy. The observed efficiency of CAESAR is shown in Fig 4.14, where it is compared to the efficiency determined by simulation.

4.4.3 GEANT4 Simulations

For the analysis, it is necessary to know the efficiency of CAESAR between the energies provided by the source run and how the doppler shift will effect the resolution and efficiency of CAESAR. A GEANT4 simulation Baugher (2012) was used to determine the in-beam efficiency and resolution of CAESAR. The simulation models the effects of energy thresholds, energy resolution, γ-ray energy, velocity, addback, Doppler shift, Compton scattering, and pair production. Furthermore, certain aspects of the experimental setup are included such as the beam pipe, detector housing, and energy loss of the projectile in the target. As shown in Fig 4.14, the simulated source efficiencies are in good agreement to the efficiencies measured with source runs during the experiment. In addition to using the simulation for efficiency values, the γ rays fit in the measured data were compared to simulated spectra. This was particularly useful at high energies where pair production and Compton scattering become significant.

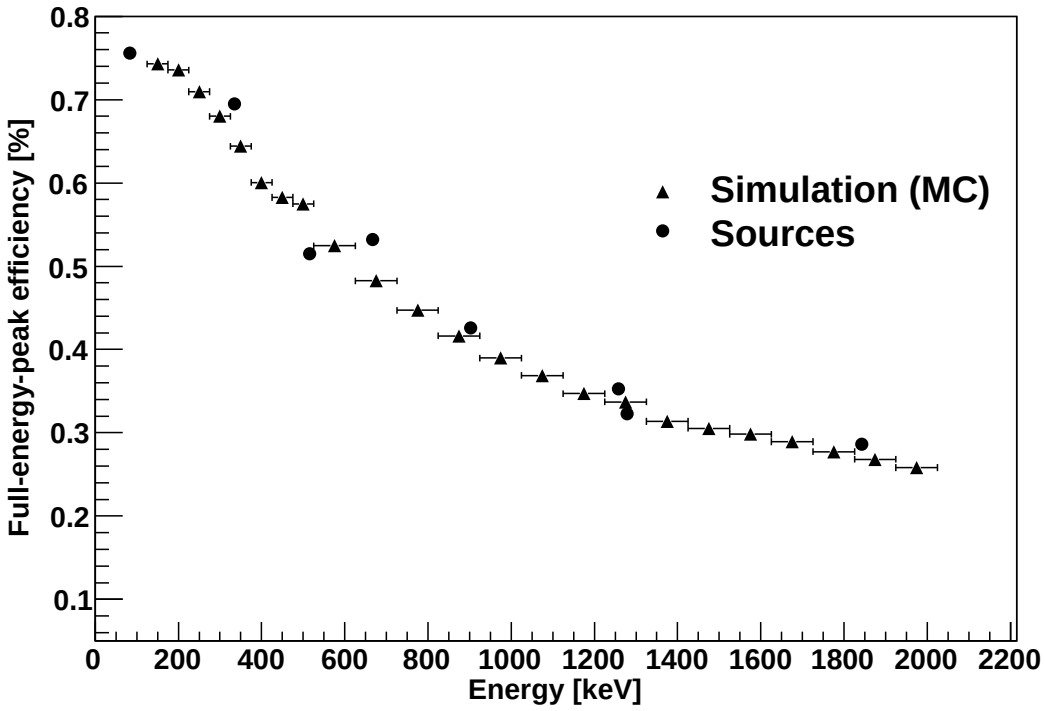

Figure 4.14: The efficiency of CAESAR at detecting γ rays at a variety of energies is shown. The efficiency shown represents the efficiency for a stationary source using the addback routine discussed in Sec 3.6.1.

Chapter 5

Analysis

The analysis of the ^{108}Sn and ^{106}Sn data are discussed in detail. This includes identifying the reaction fragments, distinguishing between knockout channels to the ground state versus excited states, extracting momentum distributions, and calculating cross sections. Discussion of the results will be reserved for Chapter 6.

5.1 Incoming Beam and Particle Identification

Particles were detected in the focal plane of the S800 spectrograph on an event-by-event basis. The particles were identified using their time-of-flight (TOF) and energy loss measurements. As discussed in Sec 3.5.3, the TOF is the difference between the e1 and xfp scintillator timing signals and provides a measure of the magnetic rigidity. The energy loss was measured in the ionization chamber (Sec 3.5.2) and allows for the discrimination of particles by charge. By utilizing the TOF and energy loss measurements, unambiguous particle identification can be achieved.

5.1.1 Unreacted Secondary Beam

Prior to the experiment, the secondary beam is directed to the S800 focal plane without a target present in the target chamber. This beam is called the unreacted

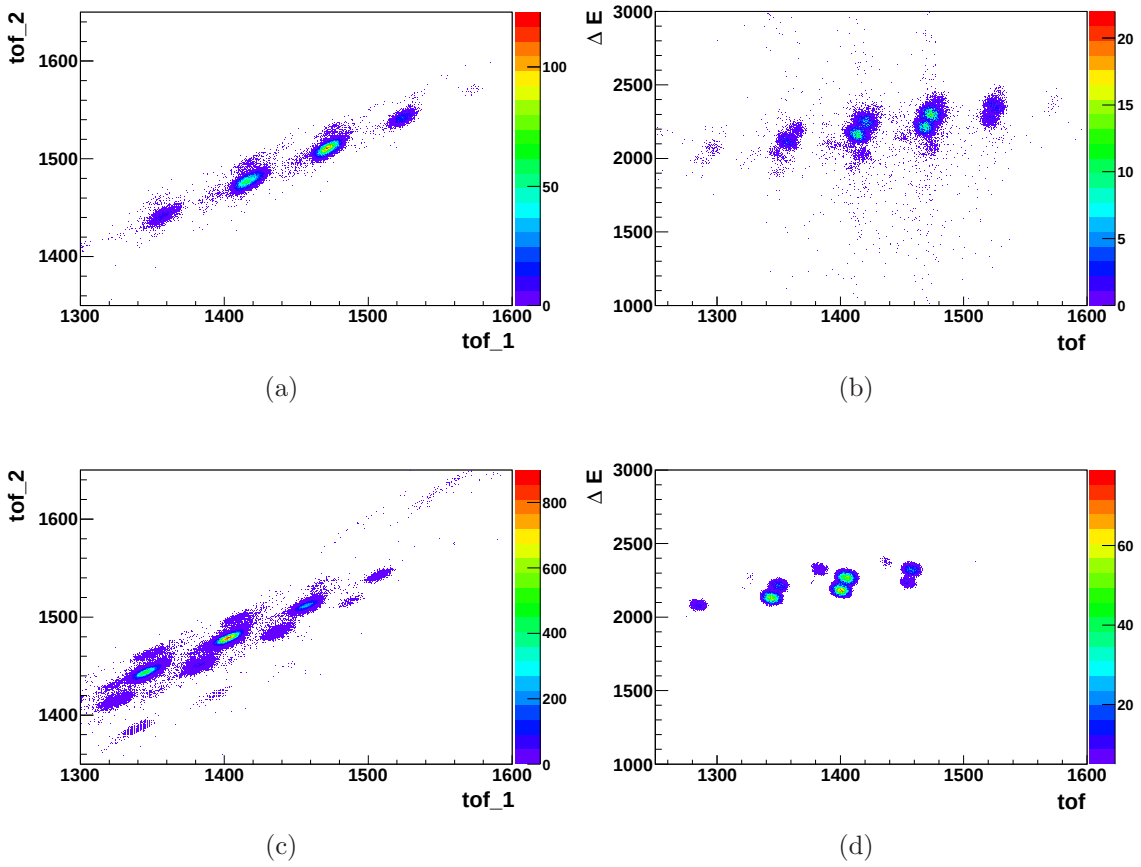

Figure 5.1: The unreacted beams for the ^{108}Sn, (a) and (b), and ^{106}Sn, (c) and (d), experiment are shown. (a) The TOF using the xfp scintillator is plotted against the TOF from the obj scintillator. This plot demonstrates that the incoming beam is made up of four discernible magnetic rigidities. (b) The xfp TOF is plotted against the energy loss to provide particle identification (PID). Here, charge states are clearly visible that cannot be resolved by magnetic rigidity alone. (c) and (d) The ^{106}Sn beam has more isotopes and charge states than the ^{108}Sn beam.

beam and is used to configure the magnet settings for the S800. The unreacted beam provided to the ^{108}Sn and ^{106}Sn experiment can be seen in Fig 5.1. The TOF vs TOF spectra provide a way to isolate reaction products based on the incoming isotope from which it came. As shown, the unreacted beam contains isotopes of tin, indium, cadmium, and silver. In addition, the PID spectra show that there are ions in dfferent charge states, but with a similar TOF (rigidity). These charge states cannot be resolved in the TOF vs TOF spectra.

5.1.2 Reacted Secondary Beam

The reacted beams can be seen in Fig 5.2. As expected, the target introduces a noticeable TOF spread compared to what was seen in Fig 5.1. Due to energy loss in the target, the reaction products will take different paths through the spectrograph portion of the S800 (after the target) dependent on their magnetic rigidity. This path difference introduces a smearing effect in the TOF. It is important to note that the TOF is dependent on the rigidity of both the projectile and reaction product. This makes it possible to distinguish between events where different projectile isotopes result in the same reaction product.

Beam particles often pass through the target without colliding. This results in a significant portion of the PID being made up of unreacted particles. As seen in panels (b) and (d) of Fig 5.2, these unreacted particles make it difficult to resolve the reaction isotope of interest. Since unreacted particles do not have nuclear interactions with the target, these particles are far less likely to be in coincidence with γ-rays. Taking advantage of this, Fig 5.3 is the result of plotting the PID for ^{108}Sn and requiring a coincident γ-ray. The number of unreacted beam particles is greatly reduced and each isotope is clearly visible. The coincidence requirement is used only for producing the plot to show more clearly the location of the reaction products. It is useful for visual purposes and knowing where to place gates. It cannot be used to clean up or eliminate data from the rest of the analysis because reaction products are not always in coincidence with a γ-ray. Often, the reaction product is in the ground state and no γ-ray is produced. The γ-ray detectors are also not 100% efficient at detecting the γ-rays (see Sec 4.4.2). This means that even if the reaction product is in an excited state, the γ-ray can simply be missed by the detectors.

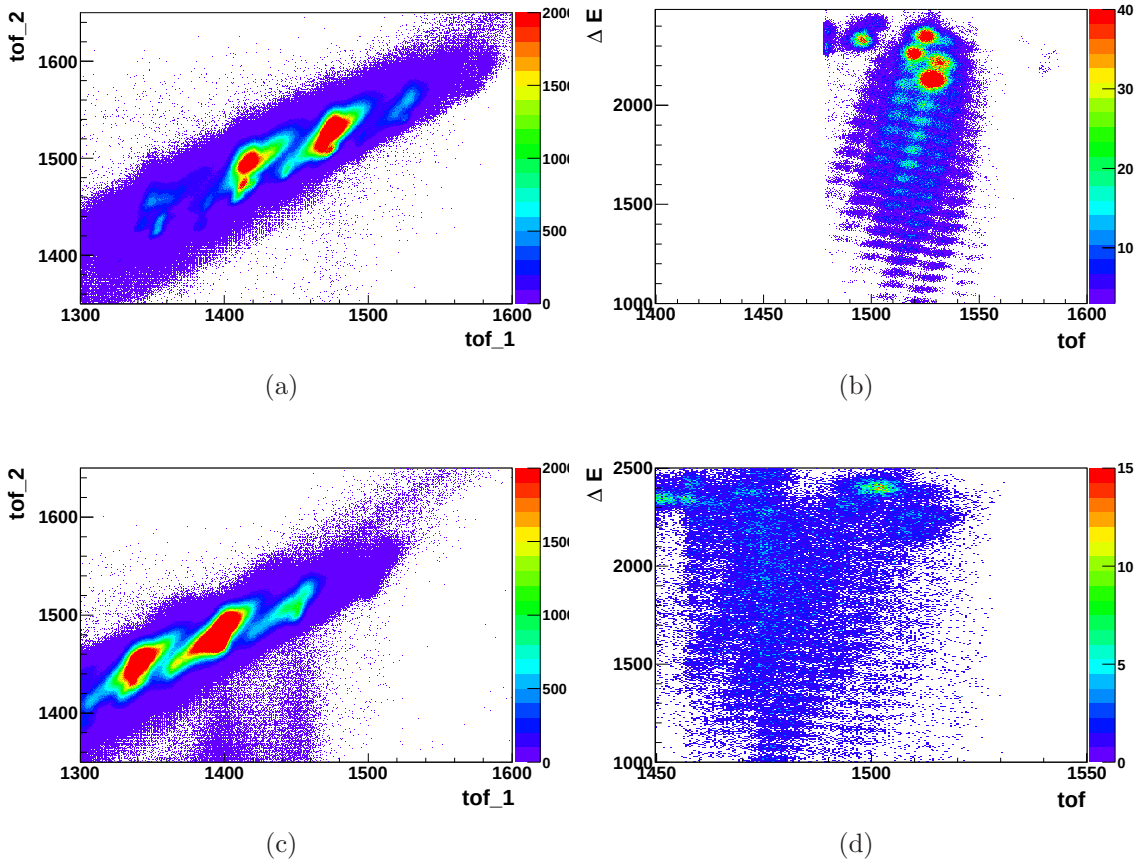

Figure 5.2: The reacted beams for the ^{108}Sn, (a) and (b), and ^{106}Sn, (c) and (d) experiment are shown. (a) The TOF vs TOF spectra has been significantly smeared as a result of the target but the incoming beams can still be resolved. (b) The unreacted particles of the beam dominate the PID and make it difficult to resolve the isotopes of interest. Despite this, many reaction products are still visible. (c) Again, the TOF vs TOF spectra has been smeared due to the target. The contaminants seen at 1400 and 1450 do not interfere with the analysis because their TOF does not overlap the area of interest. (d) The unreacted particles are again dominant but do not pose as large of a problem as in the ^{108}Sn. The reaction products of interest are resolved.

5.2 Gamma Spectroscopy

The in-beam γ-ray spectroscopy was performed using CAESAR (Sec 3.6). By measuring γ-rays, isotopes can be identified according to their γ spectra. Plotting γ-rays in coincidence with the particles in an isotope gate of the PID (Fig 5.2) results

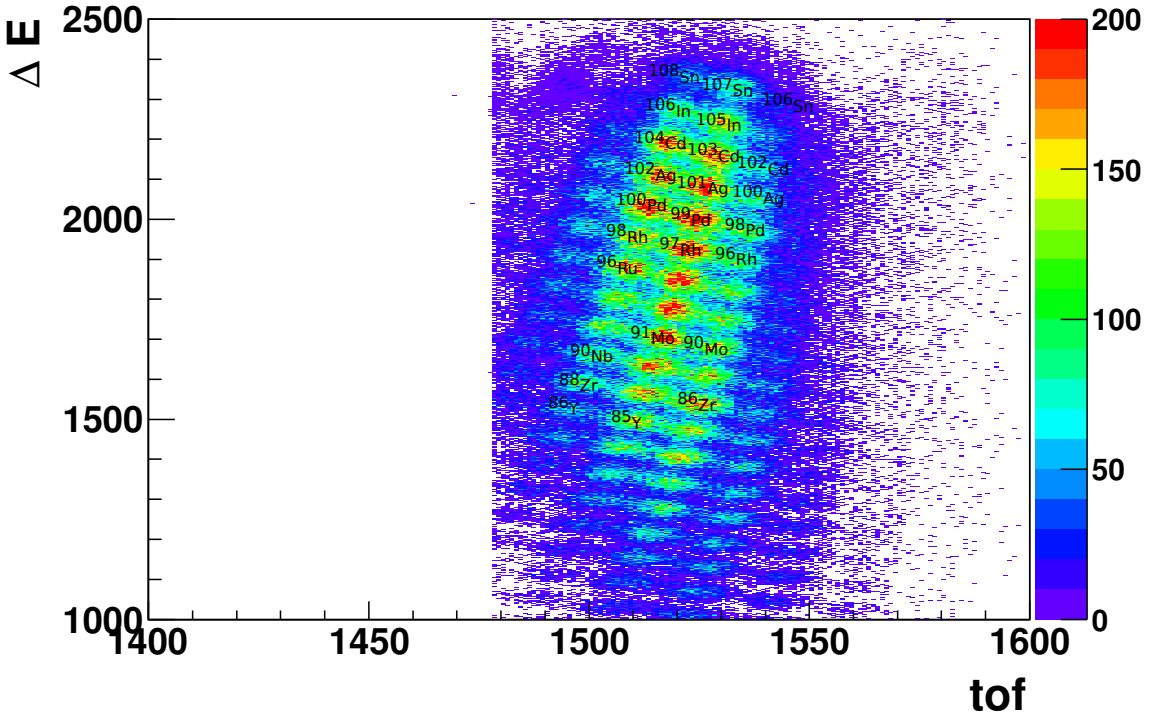

Figure 5.3: The PID for the incoming ^{108}Sn beam is shown with a γ-ray coincidence requirement. The result is that the contribution from unreacted particles is greatly reduced and the reaction isotopes are easily resolved. Isotopes in white can be identified by γ-ray spectroscopy as described in Sec 5.2.

in a γ-ray spectrum for that reaction. This spectrum is then compared to the known γ-ray transtitions of isotopes until a match is found.

Fig 5.4 shows the γ-ray spectra for ^{107}Sn and ^{105}Sn. The data has been fit using the Maximum Likelihood method described in Appendix A. The ^{107}Sn and ^{105}Sn isotopes are identified by their 150 keV and 200 keV transitions associated with their respective first excited states. In addition to the data points and the fit, simulated γ-ray peaks (Sec 4.4.3) are shown on the horizontal axis. The resolution and shape of the simulated peaks are compared to the fits to aid the interpretation of the data. The consistency between the simulation and experimental data was checked with the source runs.

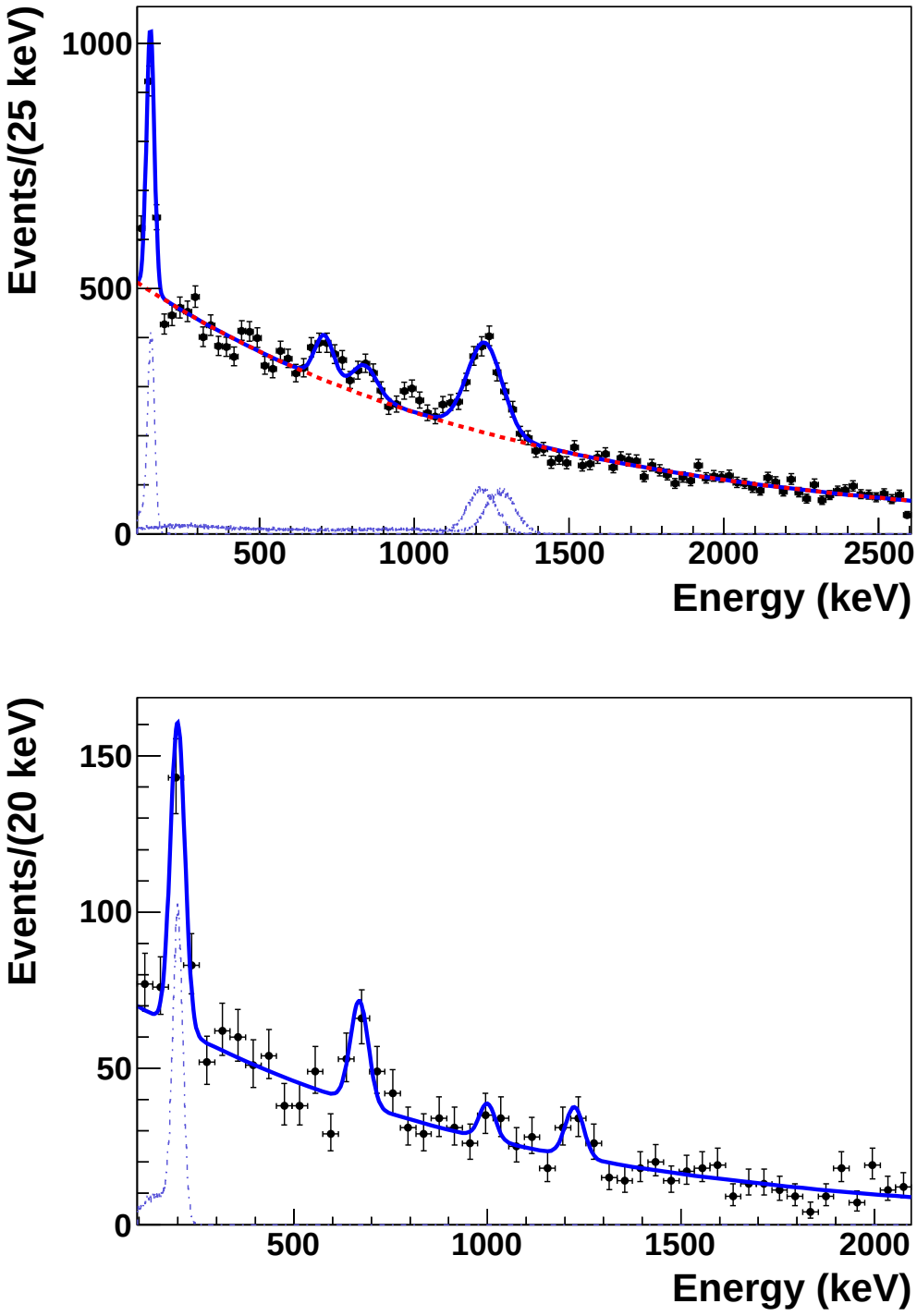

Figure 5.4: Low-energy γ-ray spectra gated on ^{107}Sn (top) and ^{105}Sn (bottom) fragments following reactions on ^{108}Sn and ^{106}Sn beams respectively. On the x-axis, simulated spectra have been plotted for specific γ-ray transitions. The data have been fit using the Maximum Likelihood method.

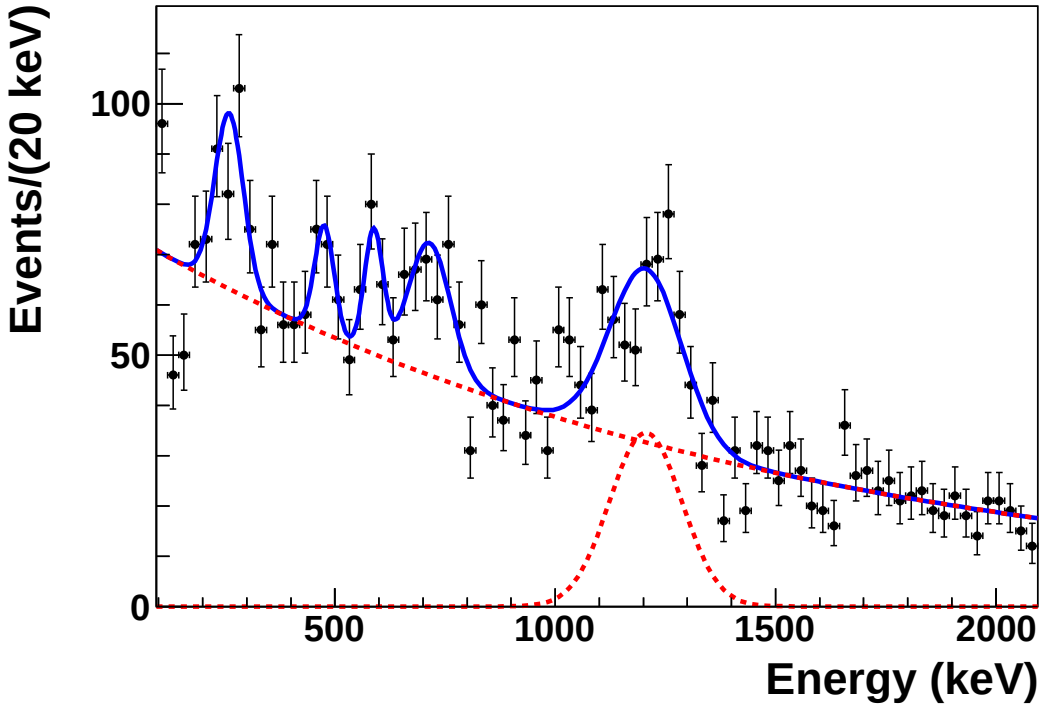

Figure 5.5: The γ-ray spectrum in coincidence with the 150 keV peak in ^{107}Sn is plotted. A strong coincidence can be seen with a 1220 keV γ-ray.

5.2.1 Coincident Gamma Rays

In order to determine the cross section for knockout to the first excited state, it was necessary to quantify the feeding from higher states, by accounting for the γ-rays in coincidence with the first excited state. Fig 5.5 shows that there is a strong 1220 keV peak in coincidence with the 150 keV first excited state in ^{107}Sn. This implies that there is strong feeding which must be accounted for when looking at the momentum distribution and calculating the cross sections. Examination of the ^{107}Sn γ-ray spectrum (Fig 5.4) revealed that all of the 1220 keV peak fed into the 150 keV first excited state. The number of events in the 1220 keV peak was corrected for the efficiency of CAESAR and subtracted from the number of events in the first excited state.

5.3 Momentum Distribution

5.3.1 Momentum Distribution Reconstruction

As described in Sec. 3.5.1, the CRDCs provide a particle position measurement in the x (dispersive) and y (non-dispersive) directions at two positions along the beam axis. The corresponding dispersive (a_{fp}) and non-disperive (b_{fp}) angles are given by:

$$\begin{aligned} a_{fp} &= \frac{\tan^{-1}(x_2 - x_1)}{1073} \\ b_{fp} &= \frac{\tan^{-1}(y_2 - y_1)}{1073} \end{aligned} \tag{5.1}$$

where x_1 (x_2) and y_1 (y_2) are the positions provided by CRDC1 (CRDC2), and 1073 is the distance in millimeters between the two CRDCs.

In order to reconstruct the momentum distribution, the fragment positions at the focal plane must be related to the corresponding positions and angles at the target position. An inverted matrix map of the dipole and quadrupole magnets is generated using the COSY INFINITY code Makino and Berz. (1999) and used to reconstruct the trajectory of a particle through the S800 Spectrometer.

The energy of a particle traversing the central trajectory of the S800 is calculated using the formula:

$$E_0 = (m)(u)\left(\sqrt{\left(\frac{B\rho_0}{3.107}\frac{q}{m}\right)^2 + 1} - 1\right) \tag{5.2}$$

where m is the mass and q the charge of the particle, u is the atomic mass, $B\rho_0$ is the magnetic rigidity of the spectrometer along the central trajectory, and 3.107 is a unit conversion factor. The trajectory reconstruction with the inverse map results in the new variables a_{ta}, y_{ta}, b_{ta}, and d_{ta}, where a_{ta} is the dispersive angle at the target,

y_{ta} is the non-dispersive position at the target, b_{ta} is the non-dispersive angle at the target, and

$$d_{ta} = \frac{E - E_0}{E_0} \tag{5.3}$$

where E is the energy of the event particle.

The d_{ta} and E_0 are used to calculate E using Eq. 5.3. The linear momentum is calculated according to the equation:

$$p = E\sqrt{1 + 2\left(\frac{(m)(u)}{E}\right)} \tag{5.4}$$

and the scattering angle is calculated according to the equation:

$$\theta = \sin^{-1}\sqrt{(\sin a_{ta})^2 + (\sin b_{ta})^2}. \tag{5.5}$$

Finally, the parallel momentum can be calculated using the formula:

$$p_{par} = p\cos\theta \tag{5.6}$$

5.3.2 Momentum Distribution Corrections

The PID does not provide absolute isotope identification. This can be seen clearly in Fig 5.2 where neighboring isotopes intrude on the ^{107}Sn and ^{105}Sn isotopes. After calculating the momentum distribution for an isotope, it is necessary to correct for the intrusion of the neighboring isotopes. The largest contribution comes from the unreacted ^{108}Sn and ^{106}Sn beams. This is due to their relatively large number of events and that they are distinguished between the ^{107}Sn and ^{105}Sn isotopes by the TOF of the particles which has a much larger deviation than the ΔE measurement in the ionization chamber. It is necessary to calculate the momentum distribution for these neighboring isotopes and subtract a scaled amount of the momentum distribution

representative of the amount of that isotope in the ^{107,105}Sn PID gate. The process is shown in Fig. 5.6 and makes it possible to remove the contributions from neighboring isotopes.

The momentum distribution of for each state must also take into account the feeding from any higher-lying coincident γ-ray peaks. As shown in Sec 5.2.1, the 150 keV first excited state of ^{107}Sn is in coincidence with a 1220 keV γ-ray. Therefore, to get the first excited momentum distribution it is necessary to subtract the feeding from this higher excited state. Similarly, the momentum distribution for the ground state can be determined by subtracting the momentum distribution of all excited states from the total momentum distribution of the isotope. The contributions from all excited states must be adjusted for the effieicency of CAESAR at that energy. The final ground state and first excited state momentum distributions for ^{107}Sn and ^{105}Sn, once all other contributions have been removed, are shown in Fig 5.7 and Fig 5.8.

5.4 Cross Sections

In order to calculate the cross sections, it is necessary to know how many ^{108}Sn and ^{106}Sn particles were supplied to the experiment. This was calculated by first finding the beam purity. For an unreacted run, the total number of ^{108}Sn and ^{106}Sn particles was divided by the total beam count in the xfp scintillator. This provided a beam purity which was multiplied by the sum of the beam counts in the xfp scintillator across all experiment runs. The result is the total number of ^{108}Sn and ^{106}Sn particles supplied to the experiment.

The cross sections are then calculated according to the equation:

$$\sigma(mb) = \frac{10^6}{0.602}\frac{A}{\rho}\frac{c}{t} \tag{5.7}$$

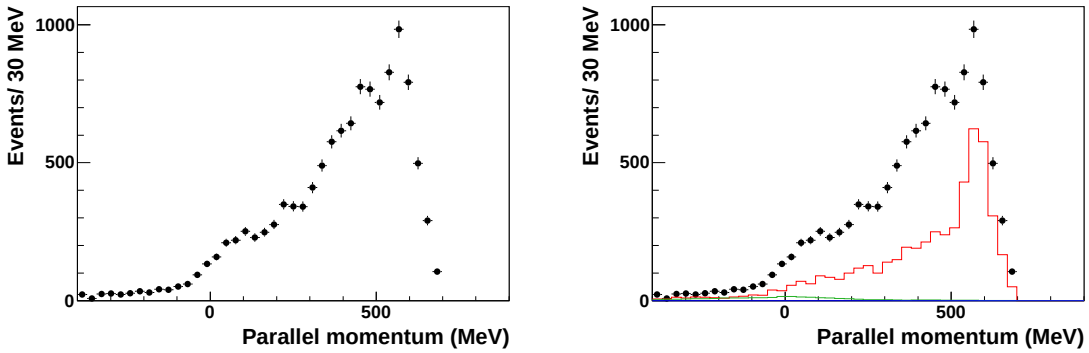

(a)

(b)

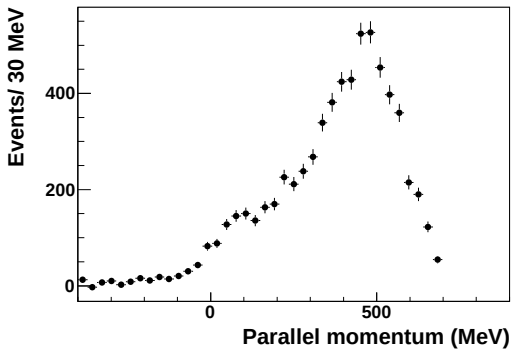

(c)

Figure 5.6: (a) The momentum distribution of ^{107}Sn ground state. (b) The same momentum distribution plotted with the scaled neighboring isotopes ^{108}Sn, ^{106}In, and ^{105}In also plotted. (c) The final momentum distribution of ^{107}Sn after subtracting the contributions from the neighboring isotopes.

Table 5.1: Experimentally determined cross sections for ^{107}Sn and ^{105}Sn are shown.

	^{107}Sn Ex σ (mb)	^{105}Sn Ex σ (mb)
Inclusive	57 ± 5	31 ± 10
Ground State	14 ± 6	< 39
First Excited	4 ± 2	3 ± 1
Through States at 1300 keV	40 ± 5	

where the leading numbers are unit correction factors, A is the mass of the target, ρ is the density of the target in mg/cm^2, t is the total number of particles previously discussed, and c is the number of counts in the corresponding final state. Cross sections were calculated for the ground state, first excited state, higher excited states, and the inclusive cross sections (all one-neutron knockout channels regardless of resulting state). An upper limit on the direct population of each state was taken from the singles γ-ray spectra. In order to take into account the feeding from higher states, the coincident γ-rays were examined closely. The calorimeter, the energy sum of all *gamma*-rays in an event, is shown in Fig 5.9 and was used to place a lower limit on the direct population of the first excited states. These spectra do not show signficant direct population of higher excited states. This may indicate feeding from higher unseen states. The results are shown in Table 5.1

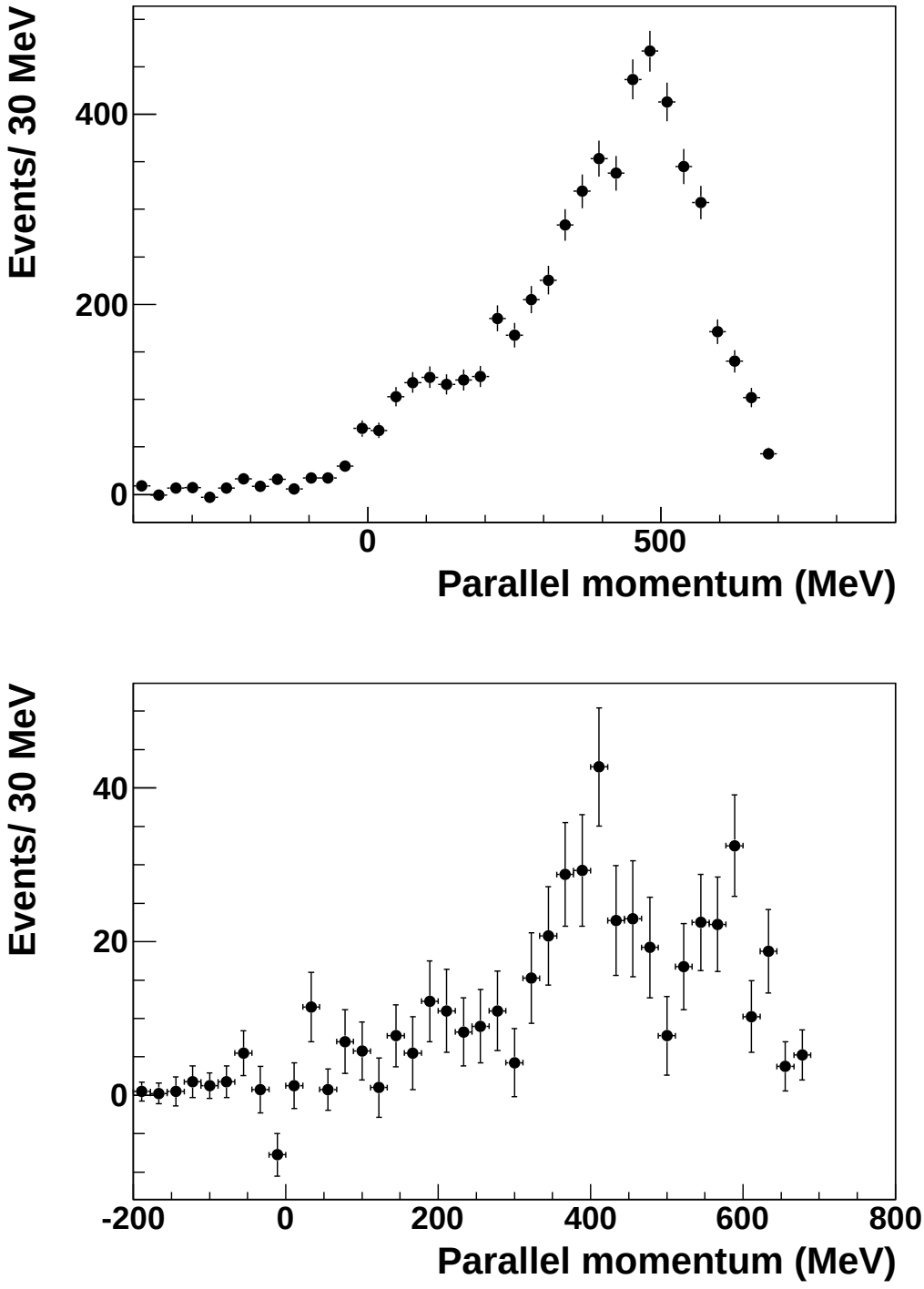

Figure 5.7: (top) The final momentum distribution for the ground state of ^{107}Sn fragment following reaction on ^{108}Sn beam. (bottom) The final momentum distribution for the first excited state of ^{107}Sn fragment following reaction on ^{108}Sn beam.

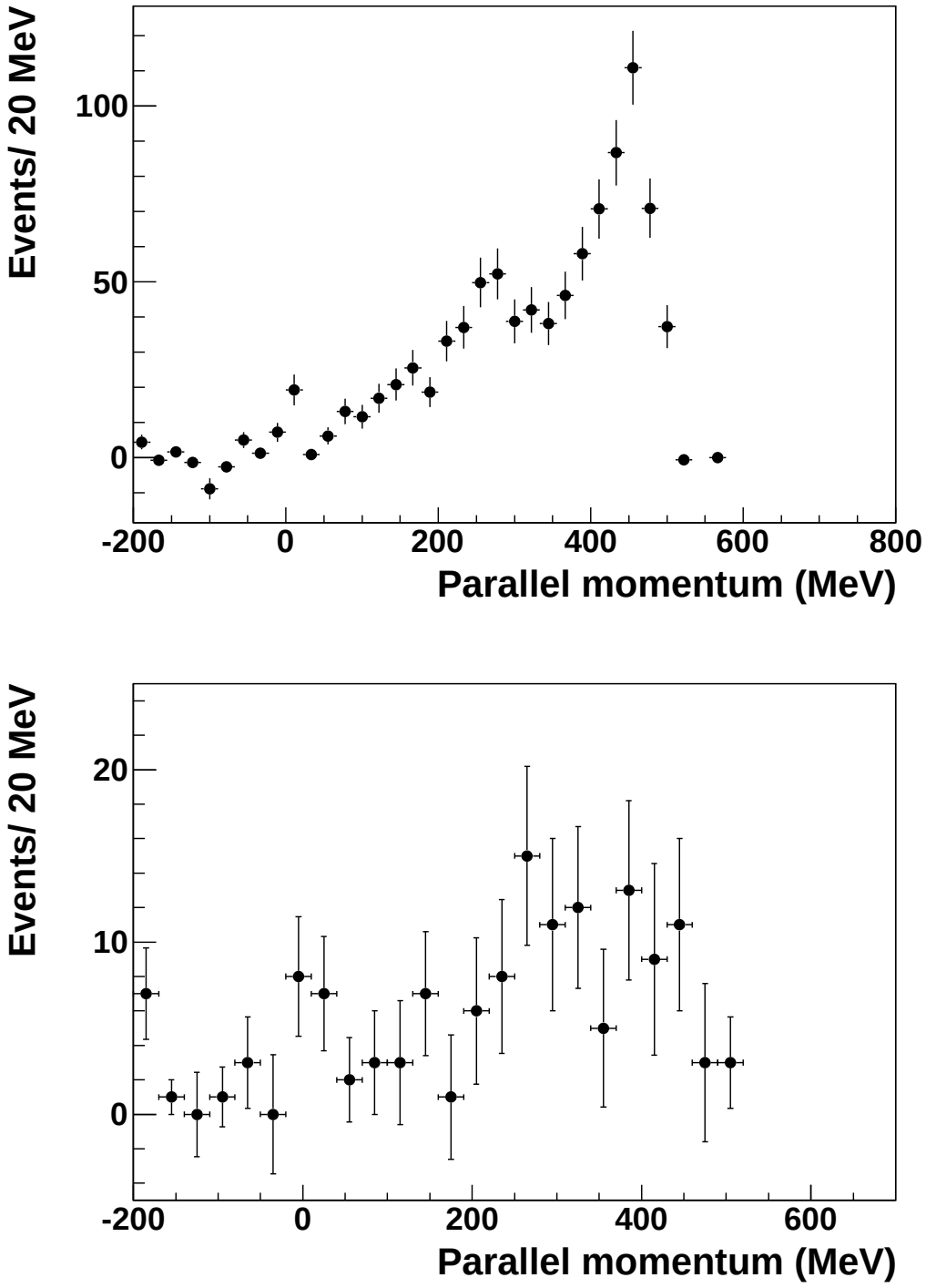

Figure 5.8: (top) The final momentum distribution for the ground state of ^{105}Sn fragment following reaction on ^{106}Sn beam. (bottom) The final momentum distribution for the first excited state of ^{105}Sn fragment following reaction on ^{106}Sn beam.

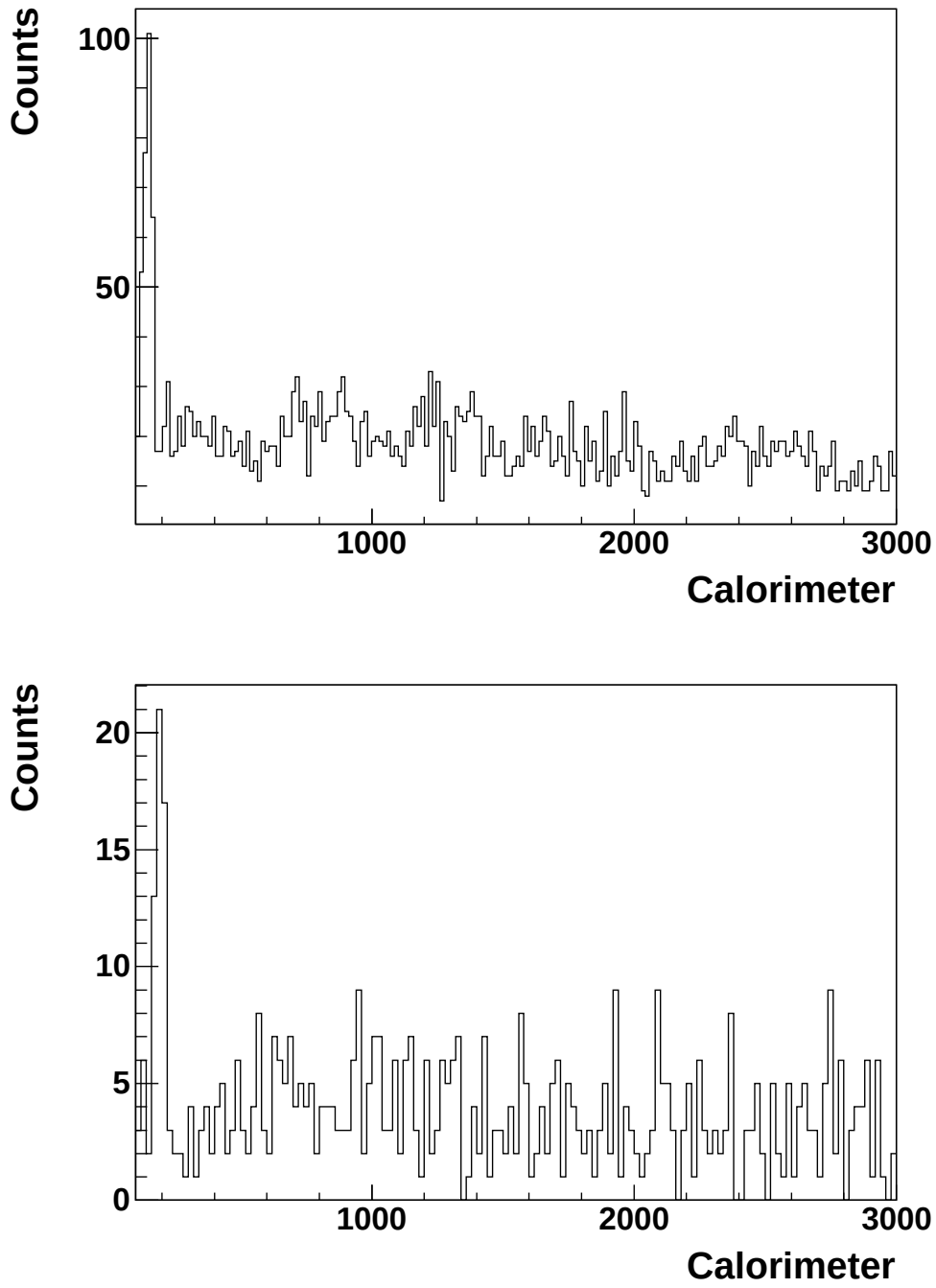

Figure 5.9: The calorimeter is the sum of all γ-rays in a single event. The ^{107}Sn (top) and ^{105}Sn (bottom) calorimeters provide a lower limit on the cross section for knockout to the first excited state.

Chapter 6

Interpretation

In Chapter 5, the γ-ray spectra and momentum distributions associated with the one-neutron knockout reaction on beams of ^{108,106}Sn were presented. Here, the interpretation of the γ-ray spectra is discussed, the momentum distributions are compared to theoretical calculations to make spin-parity assignments, and measured cross sections are presented for the various knockout channels.

6.1 Gamma Rays

The shell model discussed in Sec 2.1 can be simplified in the tin region above N=50. The near degeneracy of the $d_{5/2}$ and $g_{7/2}$ orbitals and large separation energy between these and the higher states allows us, in a simple picture, to assume that the valence neutrons will fill only the $d_{5/2}$ and $g_{7/2}$ orbitals. These neutrons are more weakly bound for light tins than those in the closed core. Thus, in a naive view of the one-neutron knockout reaction, the removed neutron will always be one of these valence neutrons. If this were the case, the reaction residue following a one-neutron knockout would always be in either the ground or first excited state. However, the measured γ-ray spectra in Sec 5.2 contain γ-ray peaks other than the first excited peak. Additionally, Sec 5.2.1 shows that γ-rays from the first excited state are seen

in coincidence with other γ-ray peaks. Indicating that this state is sometimes fed from higher states. The high energy γ-ray spectra are examined for possible sources of this feeding.

The first escape peak (Sec 3.6) in the high energy γ-ray spectra of ^{107}Sn and ^{105}Sn becomes significant and the Doppler broadening is large. The result is that the large Doppler broadening causes the full energy and first escape peaks to overlap. Therefore, γ-ray transitions have a complex shape in this region. Here, the GEANT4 simulation is a valuable tool for interpreting the high energy γ-rays. Fig 6.1 shows the high energy γ-ray spectra that is fit using the simulated shape. The ^{107}Sn spectrum shows a hint of a high energy γ-ray, but too little to make further interpretation on this alone. However, the coincidences with 1220 keV γ-rays, coupled with the hint of a high energy γ-ray, provides strong evidence that the naive view of the one-neutron knockout reaction is incorrect. The presence of these additional γ-ray peaks and feeding is interpreted here to be the result of knocking a neutron out of the ^{100}Sn core, below N=50, instead of removing a valence neutron. The removal of a neutron from the ^{100}Sn core leaves the residue in a highly excited state. This highly excited state decays to the state associated with the 1220 keV γ-ray which subsequently decays to the first excited state. This interpretation adequately explains the possible high energy γ-ray, the 1220 keV γ peak, and the coincidences seen with the first excited state.

6.2 Momentum Distributions and Cross Sections

In order to make spin-parity assignments, the momentum distributions in Sec 5.3 are compared to the momentum distributions calculated from the eikonal model by Tostevin (2013) (Sec 3.1). The calculated distributions provided do not take into account the resolution of the S800 CRDCs. Therefore, it was necessary to determine

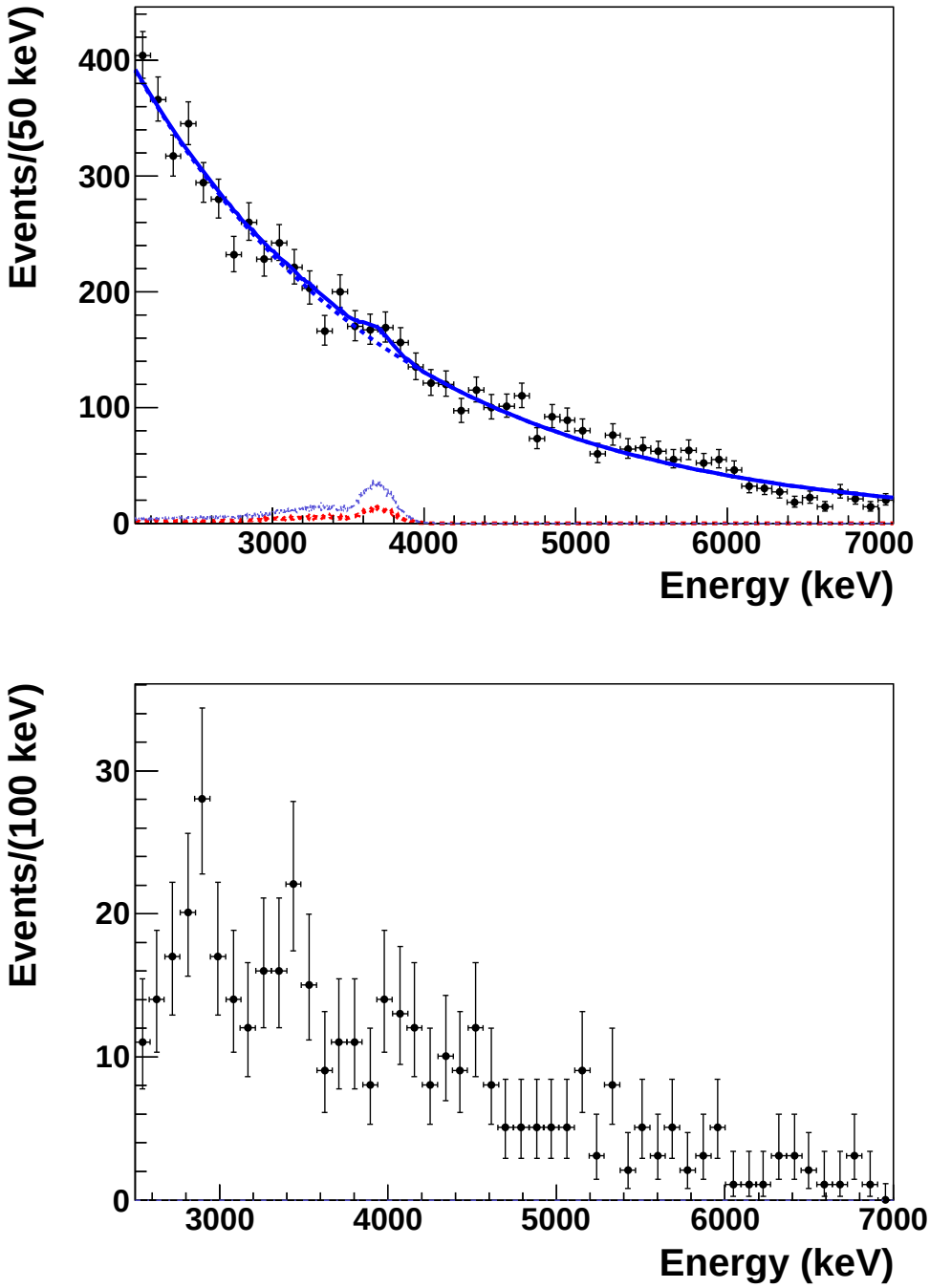

Figure 6.1: The high energy γ-rays are plotted for ^{107}Sn (top) and ^{105}Sn (bottom). The ^{107}Sn shows hints of a high energy γ-ray transition. The ^{105}Sn suffers from low statistics and makes fitting unreliable.

the resolution using the unreacted ^{108}Sn and ^{106}Sn beams then fold this resolution into the calculations with a convolution. These convoluted calculations are compared to the experimental momentum distributions in Figs 6.2-6.5.

In Fig 6.2, the momentum distribution for the ground state of the ^{107}Sn following a one-neutron knockout from ^{108}Sn is compared to the calculated distributions for $\Delta\ell = 2$ (top) and $\Delta\ell = 4$ (bottom) neutron knockout. Here, there is an asymmetry of the experimental peak which gives rise to a tail on the lower momentum side. This is the result of the reaction residue elastically scattering on the target. The scattering transfers momentum from the residue to the target and gives rise to the low momentum tail Bertulani and Hansen (2004). Therefore comparisons are made to the central and high momentum portions of the distributions. This interaction is not taken into account in the eikonal model calculations. When comparing the experimental to the calculated momentum distributions, the width of the peak is of primary importance. The calculation assuming knockout of a $d_{5/2}$ neutron provides a good fit to the experimental data for ^{108}Sn to the ground state of ^{107}Sn with the exception of the previously mentioned tail. When compared to the $g_{7/2}$ calculation, the experimental distribution is much too narrow. Therefore, the ground state of ^{107}Sn has been assigned a spin-parity of $5/2^+$. In Fig 6.3, the momentum distribution from ^{108}Sn going to the first excited state of the ^{107}Sn following a one-neutron knockout reaction has been compared to the same calculated momentum distributions as in Fig 6.2. The $\ell = 2$ (top) calculation provides a poor fit to the data. When scaled to correctly match the width of the data, it is much too large and does not have the proper shape. However, the $\ell = 4$ calculation fits the experimental distribution excellently. Thus, the first excited state of ^{107}Sn has been assigned a spin-parity of $7/2^+$.

In Fig 6.4, the momentum distribution for the ground state of ^{105}Sn following a one-neutron knockout from ^{106}Sn is compared to the calculated distributions assuming

$\Delta\ell = 2$ (top) and $\Delta\ell = 4$ (bottom) neutron knockout. Here the high momentum residues were outside the range of the S800 focal plane which resulted in a very sudden drop off in the experimental data. For this reason, the comparison is made using the visible left side of the peak. This makes comparison more difficult than for the ^{107}Sn, however there is slight preference to the $\ell = 2$ calculation as the $\ell = 4$ calculation is too wide. Therefore, the ground state of ^{105}Sn has been assigned a spin-parity of $5/2^+$. A comparison between the momentum distribution going to the first excited state of ^{105}Sn, following a one-neutron knockout, and the same calculations are made in Fig 6.5. The statistics here are much lower than in the previous comparisons and the high momentum particles are out of the S800 focal plane. However, the γ-ray tag creates cleaner experimental data and comparison with calculation is easier than for the ground state. The $\ell = 2$ calculation does not accurately fit the data as it is too narrow. The $g_{7/2}$ calculation provides a good fit to the data. The first excited state of ^{105}Sn has been assigned a spin-parity of $7/2^+$, supporting the interpretation of a $5/2^+$ ground state for ^{105}Sn.

A summary of the spin-parity assignments are given in Tab 6.1. These assignments are in agreement with the shell model calculations which were discussed in Sec 2.1 and Darby et al. (2010).

The experimentally determined cross sections are shown in Tables 6.2 and 6.3 alongside those provided by the spectator core eikonal model discussed in Sec 2.2. The presence of the first excited state knockout channels indicate a mixed $d_{5/2}$ and $g_{7/2}$ neutron configuration for the ^{108,106}Sn nuclei. For ^{107}Sn, the experimental inclusive cross section is larger than expected by the theoretical calculation. The experimental and theoretical ground state cross sections agree within the large uncertainty on the experimental cross section. The first excited state is much lower than the theoretical calculation. The experimental cross section for the higher excited states is approximately a factor of 4 larger than the theoretical calculation. These

Table 6.1: The spin-parity values deduced from one-neutron knockout on beams of ^{108,106}Sn are given for ground and first excited states.

	^{107}Sn	^{105}Sn
Ground State	$5/2^+$	$5/2^+$
First Excited	$7/2^+$	$7/2^+$

Table 6.2: Experimentally determined cross sections for ^{107}Sn are shown alongside those provided by theory. The inclusive cross section is the total cross section of the reaction, regardless of the knockout channel. Uncertainties are statistical.

	^{107}Sn Ex σ(mb)	^{107}Sn Th σ(mb)	Th Sp Factor
Inclusive	57 ± 5	46	
Ground State	14 ± 6	19	2.5
First Excited	4 ± 2	16	3.4
Through States at 1300 keV	40 ± 5		
All States Above First Excited		11	

discrepancies probably come from the theoretical calculation using a limited model space. The ground state and first excited state cross sections assume that there is no significant unseen high-energy transitions directly to these states. If there is significant unseen feeding to these states then this should be seen as an upper limit for the cross section. In the case of ^{105}Sn, there is good agreement between the experimental and theoretical inclusive cross sections. Low statistics prevent the analysis of the feeding to the ground state. Therefore, only an upper limit for the cross section of the ground state can be determined. Similar to the ^{107}Sn case, the first excited state cross section is much lower than expected from the theoretical calculation. The possibility of direct feeding into the ground state from an unseen high excited state makes comparison between the ground state and first excited state cross sections unreliable. Therefore, little can be said about the degree of neutron configuration mixing in the ground states of ^{108,106}Sn.

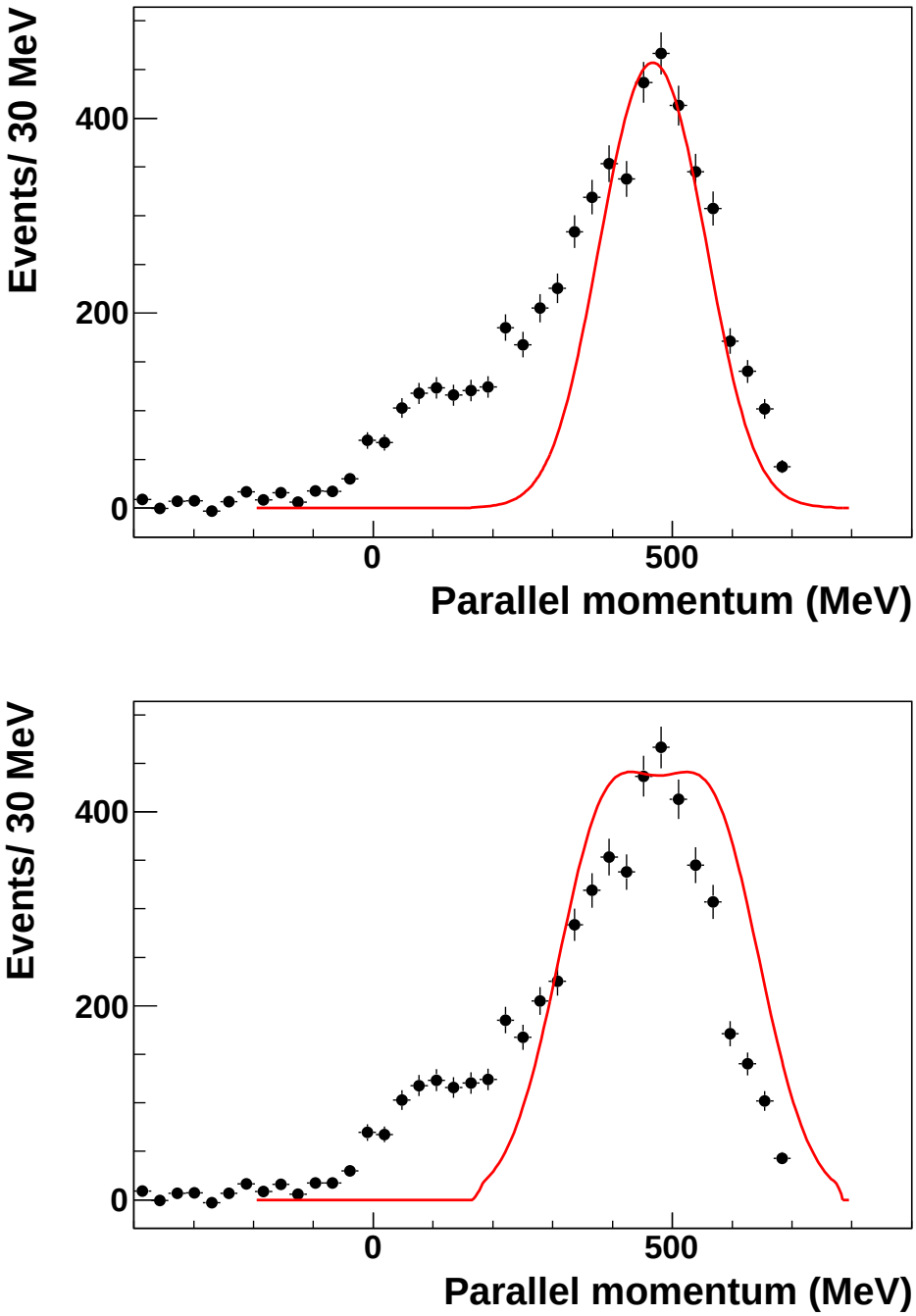

Figure 6.2: The final momentum distribution of ^{107}Sn residues in the ground state following the one-neutron knockout from ^{108}Sn is compared to theoretical calculations assuming $\ell = 2$(top) and $\ell = 4$(bottom) knockout.

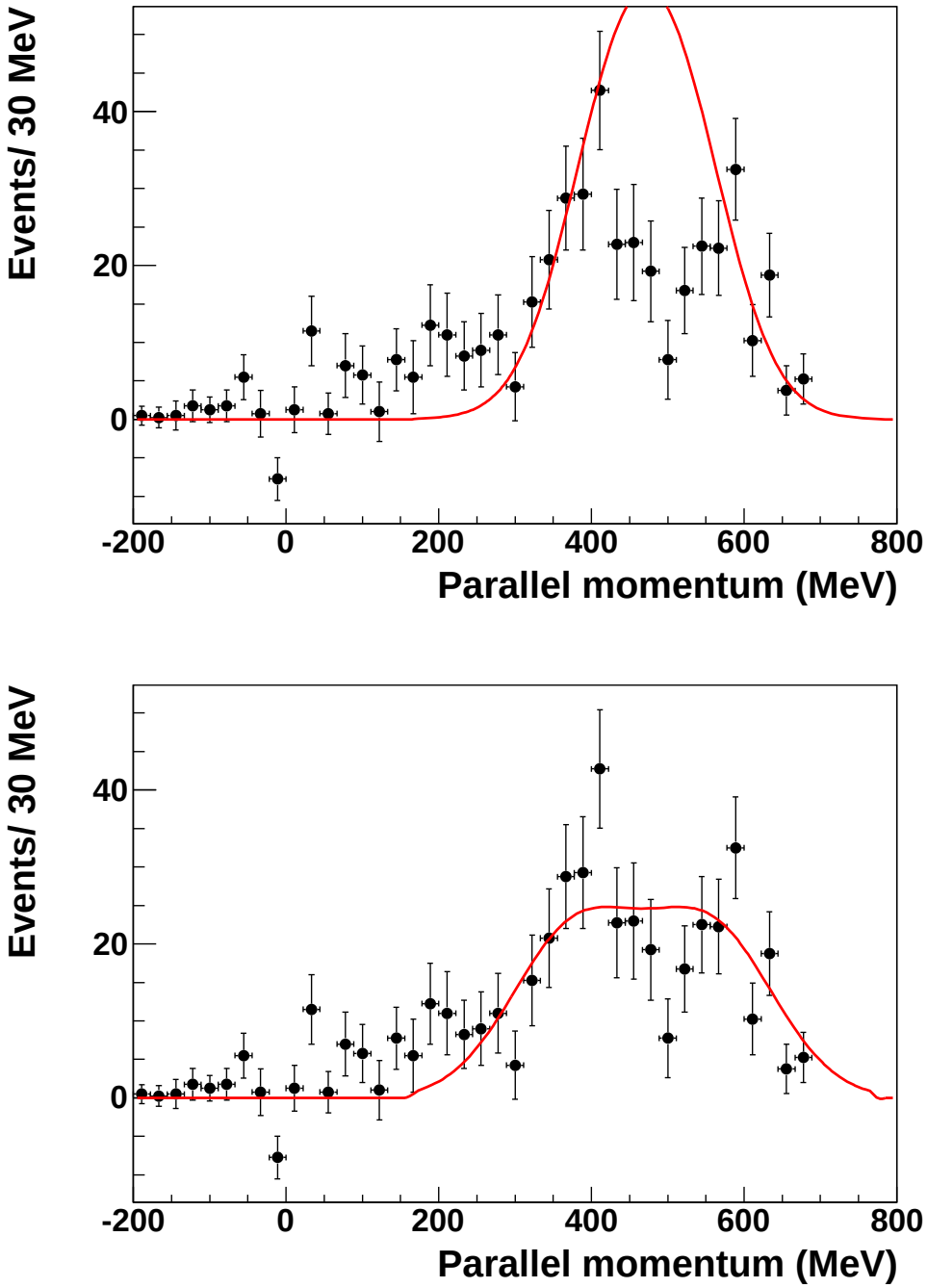

Figure 6.3: The final momentum distribution of ^{107}Sn residues in the first excited state following the one-neutron knockout from ^{108}Sn is compared to theoretical calculations assuming $\ell = 2$(top) and $\ell = 4$(bottom) knockout.

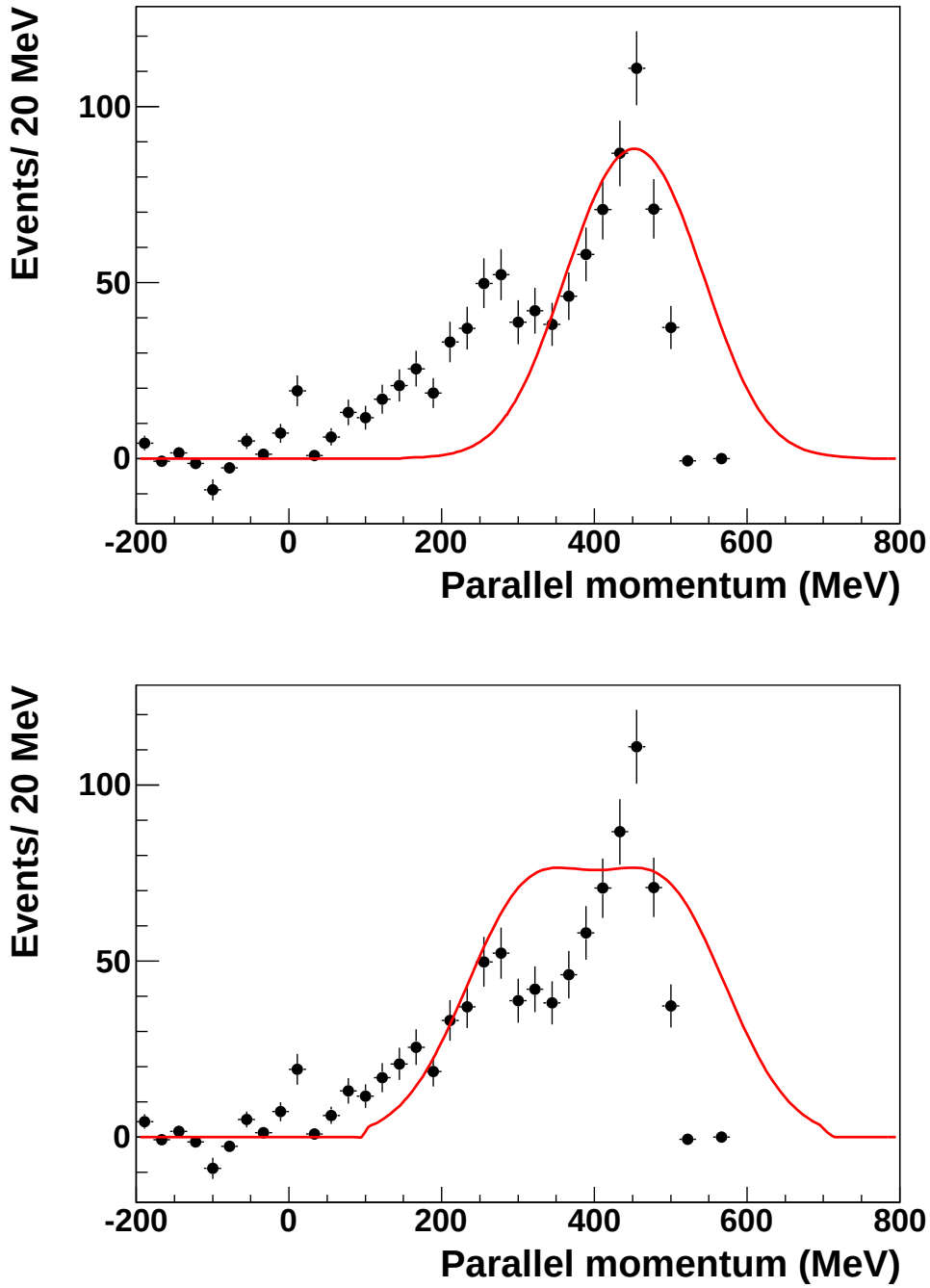

Figure 6.4: The final momentum distribution of ^{105}Sn residues in the ground state following the one-neutron knockout from ^{106}Sn is compared to theoretical calculations assuming $\ell = 2$(top) and $\ell = 4$(bottom) knockout.

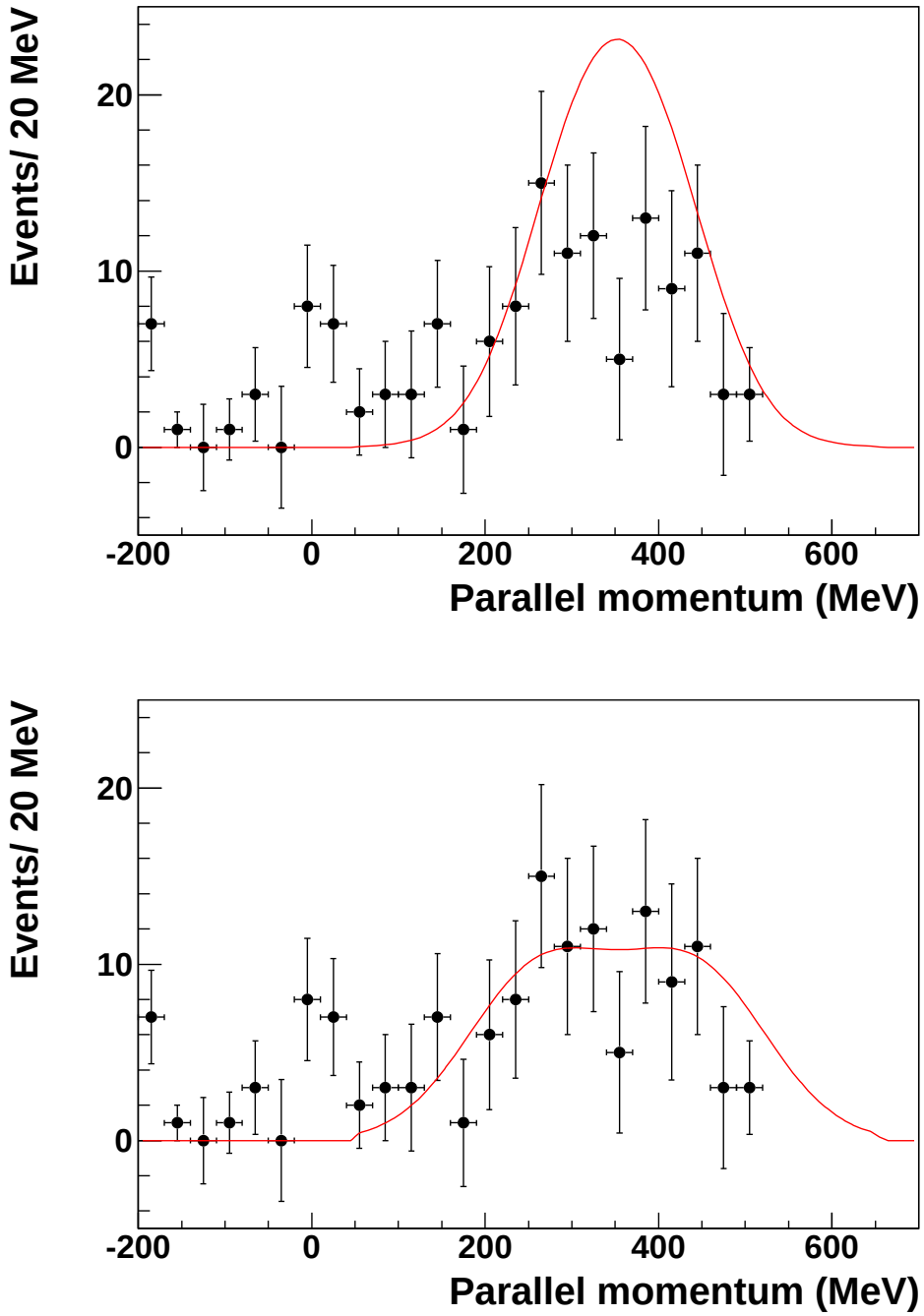

Figure 6.5: The final momentum distribution of ^{105}Sn residues in the first excited state following the one-neutron knockout from ^{106}Sn is compared to theoretical calculations assuming $\ell = 2$(top) and $\ell = 4$(bottom) knockout.

Table 6.3: Experimentally determined cross sections for ^{105}Sn are shown alongside those provided by theory. The inclusive cross section is the total cross section of the reaction, regardless of the knockout channel.

	^{105}Sn Ex σ(mb)	^{105}Sn Th σ(mb)	Th Sp Factor
Inclusive	31 ± 10	34	
Ground State	< 39	14	1.9
First Excited	3 ± 1	13	2.8
Higher Excited		7	

Chapter 7

Conclusion

The study was motivated by the need to probe the nuclear structure in the regions close to doubly magic ^{100}Sn. In February 2011, an experiment was conducted at the National Superconducting Cylotron Laboratory at Michigan State University where the one-neutron knockout reactions ^{9}Be(^{108}Sn, ^{107}Sn + γ)n and ^{9}Be(^{106}Sn, ^{105}Sn + γ)n were used to study the structure of ^{107}Sn and ^{105}Sn respectively. A primary beam of ^{124}Xe was used to produce secondary beams of ^{108}Sn and ^{106}Sn. These were reacted on a ^{9}Be target at the front of the S800 spectrograph at 140 MeV/nucleon. CAESAR was used to measure γ-rays in coincidence with the neutron knockout, allowing us to differentiate between the ground state and first excited state knockout channels. The reaction residues were then directed to the S800 focal plane. The residues were identified using the ΔE-TOF method. The x and y positions of each particle were measured using CRDCs

These positions were used to reconstruct the momentum distributions of the ^{107}Sn and ^{105}Sn reaction residues at the target. These momentum distributions were used to determine the ℓ-values of the ground state and first excited state for ^{107}Sn and ^{105}Sn. These assignments were made by comparing the experimental momentum distributions with theoretical distributions calculated from a spectator core eikonal model. This lead to a spin-parity assignment of $5/2^+$ for the ground state and $7/2^+$

for the excited state of ^{107,105}Sn. The presence of the first excited state γ-ray indicates that the configuration space of ^{108,106}Sn isotopes are mixed between the $d_{5/2}$ and $g_{7/2}$ single-particle states.

The cross sections for the knockout to the ground state are compared to those for the knockout to the first excited state. In the case of both ^{107,105}Sn, the cross section for knockout to the ground state is significantly larger than the cross section for knockout to the first excited state. This indicates that the wavefunctions for the ground state of ^{108,106}Sn are dominated by the $d_{5/2}$ single-particle state. These cross sections are also compared to reaction calculations which used as input the neutron configuration that was calculated in the shell model. In both ^{107,105}Sn, the experimental ground state cross sections are between 50% more than and twice those predicted by theory, while the experimental first excited state cross sections are significantly less than those predicted by theory. This could indicate that the $d_{5/2}$ dominates the neutron configuration more than predicted by the shell model calculations.

7.1 Future Outlook

This experiment was used to gauge the feasibility of a future one-neutron knockout experiment on ^{102}Sn and ^{104}Sn. This study has been proposed and accepted at RIKEN using the high-efficiency γ-ray detector array DALI2 in conjunction with the Zero Degree Spectrometer. The proposed experiment uses a ^{124}Xe primary beam to produce the ^{102}Sn and ^{104}Sn secondary beams. The momentum distribution of the resulting ^{101}Sn and ^{103}Sn residues reflect the ℓ-value of the removed neutron and will be measured. By measuring γ-rays in coincidence with the knockout reaction, it is possible to differentiate between knockout to the ground state from knockout to the first excited state. The momentum distributions for each knockout channel

will be compared with reaction calculations. These will be used to make spin-parity assignments to the ground and first excited states of ^{101}Sn and ^{103}Sn.

Bibliography

Bibliography

Baugher, T.: 2012, private communication. 43

Baumann, T.: 2011, Tenth exotic beam summer school: Beam optics. 20

Bazin, D.: 2012, S800 spectrograph service leve description. 21, 24, 25, 26

Bazin, D., Caggiano, J., Sherrill, B., Yurkon, J. and Zeller, A.: 1993, The S800 spectrograph, *Nucl. Instr.Meth. B* **204**, 629. xi, 21, 22

Bertulani, C. and Hansen, P.: 2004, Momentum distributions in stripping reactions of radioactive projectiles at intermediate energies, *Phys. Rev . C* **70**, 034609. 63

Darby, I., Grzywacz, R., Batchelder, J., Bingham, C., Cartegni, L., Gross, C., Hjorth-Jensen, M., Joss, D., Liddick, S., Nazarewicz, W., Padgett, S., Page, R., Papenbrock, T., Rajabali, M., Rotureau, J. and Rykaczewski, K.: 2010, Orbital dependent nucleonic pairing in the lightest known isotopes of tin, *Phys. Rev. Lett.* **105**, 162502. x, 6, 8, 12, 64

Entem, D. and Machleidt, R.: 2003, Accurate charge-dependent nucleon-nucleon potential at fourth order of chiral pertubation, *Phys. Rev. C* **68**, 041001. 7

Fahlander, C., Palacz, M., Rudolph, D., Sohler, D., Blomqvist, J., Kownacki, J., Lagergren, K., Norlin, L., Nyberg, J., Algora, A., Andreoiu, C., de Angelis, G., Atac, A., Bazzacco, D., Berglund, L., Back, T., Cederkall, J., Cederwall, B.,

Dombradi, Z., Fant, B., Farnea, E., Gadea, A., Gorska, M., Grawe, H., Hashimoto-Saitoh, N., Johnson, A., Kerek, A., Klamra, W., Lenzi, S., Likar, A., Lipoglavsek, M., Moszynski, M., Napoli, D., Rossi-Alvarez, C., Roth, H., Saitoh, T., Sewerniak, D., Skeppstedt, O., Weiszflog, M. and Wolinska, M.: 2001, Excited states in ^{103}sn: Neutron single-particle energies with respect to ^{100}sn, *Phys. Rev. C* . x, 6

Gade, A. and Glasmacher, T.: 2008, In-beam nuclear spectroscopy of bound states with fast exotic ion beams, *Prog. Part. Nucl. Phys.* **60**, 161. 17

Hansen, P.: 1996, Momentum content of single-nucleon halos, *Phys. Rev. Lett.* . 14

Hjorth-Jensen, M., Kuo, T. and Osnes, E.: 1995, Realistic effective interaction for nuclear systems, *Phys. Rep.* **261**, 125. x, 5, 7, 8

Hussein, M. and McVoy, K.: 1985, Inclusive projectile fragmentation in the spectator model, *Nucl. Phys. A* **445**, 124. 14

Lewitowicz, M., Anne, R., Auger, G., Bazin, D., Borcea, C., Borrel, V., Corre, J., Dorfler, T., Fomichov, A., Grzywacz, R., Guillemaud-Mueller, D., Hue, R., Huyse, M., Janas, Z., Keller, H., Lukyanov, S., Mueller, A., Penionzhkevich, Y., Pfutzner, M., Pougheon, F., Rykaczewski, K., Saint-Laurent, M., Schmidt, K., Schmidt-Ott, W., Sorlin, O., Szerypo, J., Tarasov, O., Wauters, J. and Zylicz, J.: 1994, Identification of the doubly-magic nucleus ^{100}sn in the reaction ^{112}sn + ^{nat}ni at 63 mev/nucleon, *Phys. Letters B* **332**, 20. 2

Machleidt, R.: 2001, High-precision, charge-dependent bonn nucleon-nucleon potential, *Phys. Rev. C* **63**, 024001. 8

Makino, K. and Berz., M.: 1999, Cosy infinity version 8, *Nucl. Instr. Meth. A* **427**, 338. 52

Mayer, M. and Jensen, J.: 1955, *Elementary Theory of Nuclear Shell Structure*, Wiley. 12

Myung, I.: 2003, Tutorial on maximum likelihood estimation, *Journal of Mathematical Psychology* **47**, 90. 80

Padgett, S.: 2011, *The Beta Decay of 79,80,81Zn and Nuclear Structure around the N=50 Shell Closure*, PhD thesis, University of Tennessee. xi, 13

Schardt, D., Kirchner, R., Klepper, O., Reisdorf, W., Roeckl, E. and Tidemand-Petersson, P.: 1979, Alpha decay studies of tellurium, iodine, xenon, and cesium isotopes, *Nucl. Phys. A* . x, 6

Schatz, H., Aprahamian, A., Barnard, V., Bildsten, L., Cumming, A., Ouellette, M., Rauscher, T., Thielemann, F. and Wiescher, M.: 2001, End point of the rp process on accreting neutron stars, *Phys. Rev. Lett.* **86**, 3471. x, 2

Schneider, R., Friese, J., Reinhold, J., Zeitelhack, K., Faestermann, T., Gernhauser, R., Gilg, H., Heine, F., Homolka, J., Kienle, P., Kurmer, H., Geissel, H., Munzenberg, G. and Summerer, K.: 1994, Production and identfication of ^{100}Sn, *Z. Phys. A* **348**, 241. 2

Sewerniak, D., Walters, W., Woehr, A., Lipoglavsek, M., Shergur, J., Davids, C., Heinz, A. and Ressler, J.: 2002, Population of the 168-kev ($g_{7/2}$) excited state in ^{103}sn in the α decay of ^{107}te, *Phys. Rev. C* . x, 6

Seweryniak, D., Carpenter, M., Gros, S., Hecht, A., Hoteling, N., Janssens, R., Khoo, T., Lauritsen, T., Lister, C., Lotay, G., Peterson, D., Robinson, A., Walters, W., Wang, X., Woods, P. and Zhu, S.: 2007, Single-neutron states in ^{101}Sn, *Phys. Rev. Lett.* **99**, 022504. x, 4, 5, 8

Stolz, A., Baumann, T., Ginter, T., Morrissey, D., Portillo, M., Sherrill, B., Steiner, M. and Stetson, J.: 2005, Production of rare isotope beams with the nscl fragment separator, *Nucl. Instr. Meth. B* **241**, 858. xi, 18, 19

Tostevin, J.: 2001, Single-nucleon knockout reactions at fragmentation beam energies, *Nuclear Physics A* **682**, 320. 14, 17

Tostevin, J.: 2013, Private communication. xi, 15, 61

Weisshaar, D., Gade, A., Glasmacher, T., Grinyer, G., Bazin, D., Adrich, P., Baugher, T., Cook, J., Diget, C., McDaniel, S., Ratkiewicz, A., Siwek, K. and Walsh, K.: 2010, Caesar - a high-efficiency CsI(Na) scintillator array for in-beam γ-ray spectroscopy with fast rare-isotope beams, *Nucl. Instr. Meth. A* **624**, 615. xi, 28

Wiringa, R., Stoks, V. and Schiavilla, R.: 1995, Accurate nucleon-nucleon potential with charge-independence breaking, *Phys. Rev. C* **51**, 38. 7

Wong, S.: 1998, *Introductory Nuclear Physics*, Wiley-VCH. 12

Appendix

Appendix A

Maximum Likelihood

The Maximum Likelihood estimation (MLE) is a fitting procedure used to estimate the parameters of a statistical model. This is accomplished by using probability density functions (PDFs) to determine the parameters which are most likely to produce the provided data.

PDFs are typically constructed from common functions (Gaussian, exponential, etc) but can be any continuous differentiable function. When fitting the high-energy γ-rays discussed in Sec 6.1, the PDF partially consisted of the probability distribution produced by GEANT4 simulation.

The PDF models the distribution of the observed data. Since the task is to determine the PDF from the observed data and not to predict the data from a given PDF, a new function must be defined. The likelihood function is defined by reversing the roles of the data vector y and the parameter vector w for a PDF such that:

$$L(w|y) = f(y|w) \tag{A.1}$$

where f(y—w) is the PDF Myung (2003).

The MLE is found by maximizing the likihood equation with respect to w_i,

$$\frac{\partial lnL(w|y)}{\partial w_i} = 0 \tag{A.2}$$

where the natural log of the likelihood function is used to make the problem less computationally expensive.

Vita

Andrew Ayres was born in Madison, TN on July 7, 1983. He went to high school in Springfield, Tn and graduated in 2002. He went on to major in Computer Science at the University of Tennessee of Knoxville. He then transitioned into Physics and began studies his graduate studies in 2008. He successfully defended his thesis on April 17, 2014 and will graduate with his Ph.D. in May 2014.